



HASP Final Flight Report 2016

Hazardous Gases for Harsh Environments LED Sensor

University of Central Florida

Report Date: December 09, 2016

Table of Contents

Abstract	3
LIST OF FIGURES	4
LIST OF TABLES	5
CHAPTER 1: Payload Description	6
1.1 Motivation	7
1.2 Principles of Operation.....	7
1.3 Payload Description	7
1.4 Scientific Objectives	8
Chapter 2: Team Structure and Management	9
2.1 Team Demographics	9
2.2 Timeline	10
CHAPTER 3: Sensor Design	11
3.1 Infrared Source	11
3.2 Component Selection and Design Details.....	11
3.3 Optical Train Optimization and Simulations	15
3.4 Driving Electronics	17
3.5 Thermal Management	19
3.6 DAQ Control.....	19
3.7 Power Specifications	20
3.8 Overall HASP Flight Design.....	22
CHAPTER 4: Validation Tests	26
4.1 Experiment Apparatuses	26
4.2 Detectability Limit, Cross Interference, and Simultaneous Measurements	26
4.3 Time Resolutions.....	29
4.4 Environmental Chamber Evaluations.....	32
4.5 HASP Integration Thermal/Vacuum Testing.....	33
CHAPTER 5: HASP Flight	35
5.1 Telemetry	35
5.2 Flight-line Setup and Pre-Launch Checkout Procedures	38
5.3 Flight Results	39
5.5 Post-Flight	41
CHAPTER 6: Conclusions and Future Work	43

6.1 Conclusion.....	43
6.2 Future Work	44
CHAPTER 7: Presentations and Publications	45
7.1 NSMMS/CRASTE Presentation	45
7.2 COE CST ATM6 Presentation.....	45
REFERENCES	46
APPENDIX: DAQ CODE (VI's)	49
FPGA Main	50
RT Main	51
Matlab Flight Data Analysis Script.....	54

Abstract

A robust and low-cost CO/CO₂ sensor has been developed for the applications of an enhanced early fire hazard detection sensor for space vehicles. However, is desirable to extend the sensor to environments outside the human habitable area of the vehicle so that the technology may be used to detect other threatening events such fuel leaks or other gas ventilation. In order to validate the technology for its suitability in this area the sensor developed for CO/CO₂ measurements will flown to high altitudes where it will encounter like conditions to these harsh environments.

LIST OF FIGURES

Figure 1: Gases Within the Spectral Region of Available MIR LEDs	6
Figure 2: Normalized spectral profiles of the LEDs (dashed lines) and filters (solid lines)	12
Figure 3 Emission spectral of the 3.6 μ m LED at different temperatures	13
Figure 4: Sensor hardware and processing schematic, including measurement flow cell.....	14
Figure 5: Pitch lens design one	15
Figure 6: Pitch lens design two.....	16
Figure 7: Simulation of the entire beam path for the 3.6 μ m LED emission.....	16
Figure 8: Simulation detector face	17
Figure 9: LED output comparison for upgraded circuit.....	18
Figure 10: The aluminum mass for the 3.6 μ m LED	19
Figure 11: Schematic depicting the sensor DAQ architecture.....	20
Figure 12: HASP EDAC516 connector interface with Sensor payload power system	21
Figure 13: LED/TEC Electronics Board as shown in Power Schematic of Figure 12	22
Figure 14: Payload attached to HASP Mechanical Interface Plate.....	23
Figure 15: Payload attachment locations on HASP Mechanical Interface Plate	24
Figure 16: Top view of payload on HASP Mechanical Interface Plate (units are in inches)	24
Figure 17: Pictures of the built system displaying the LED setup.....	25
Figure 18: Simple flow cell constructed of PVC, nylon tubing, and sapphire windows	26
Figure 19: Calibration results for (a) CO ₂ and (b) CO in the 8cm calibration cell.....	27
Figure 20: Sensitivity analysis based on the local slope of the calibration curves	28
Figure 21: Results from the cross-interference measurements	29
Figure 22: Optical chopper used for beam modulation in the temporal response studies	30
Figure 23: Temporal-resolution measurement results at (a) 250Hz, (b) 325Hz	31
Figure 24: Dr. Peale’s environmental chamber at UCF.....	33
Figure 25: Environmental testing chamber at CSBF	34
Figure 26: LED Magnitudes	39
Figure 27: Flight Profile.....	40
Figure 28: LED Output and Ambient Temperature vs. Time	41
Figure 29: Post-flight pictures showing the sheared-off optical screws	42
Figure 30: Top view of the system showing missing screws.....	42

LIST OF TABLES

Table 1: Team Personnel, Roles, and Contact Information	9
Table 2: Work Schedule by Month from January of 2016	10
Table 3: Pellicle Beam Splitter Transmittance/Reflectance	13
Table 4: Power Breakdown.....	21
Table 5: Power Breakdown for HASP System	21
Table 6: Other Relevant Power Information.....	22
Table 7: Payload Weight.....	23

CHAPTER 1: Payload Description

This payload is a system that utilizes hazardous gas sensors to ensure they operate in harsh environments. These sensors function through the use of inexpensive low-power light-emitting diodes (LEDs) in the mid-infrared (MIR) spectral range under the operating principles of direct absorption spectroscopy; the use of these principles provides time-resolved measurements of the targeted gases at the parts per million (ppm) level. These instruments are designed to fly on space vehicles which may include manned, unmanned, low Earth orbit (LEO), and interplanetary vehicles as well as space stations. The environments encountered on these vehicles will vary from having to support human life to being able to survive in the vacuum of space. The HASP 2016 balloon flight, which occurred in September of 2016, provided access to relevant conditions and allowed for demonstration of autonomous operation of the sensor.

The current sensor design targets CO and CO₂, which are trace gases that increase in the presence of smoldering or burning materials, and it is intended as an enhanced early fire hazard detection sensor for space vehicles. This sensor was designed in collaboration with and funded in part by the Federal Aviation Administration, under the Center of Excellence Commercial Space Transportation (FAA COE CST) research structure. The sensor was designed for habitable environments, however the technology series is intended to be extended beyond this environment. With compact, economical, low-power sensors capable of continuously monitoring gases that are characteristic of burning materials, a distributed sensor array could be implemented on space vehicles that would allow early detection of fires, gas leaks, or other critical events. Future sensors using this technology will target additional gases such as RP1, methane (CH₄), ammonia (NH₃), polymer vapors, and other expected vented or generated gases of space vehicles. Figure 1 shows the absorption features of some of the gases that can be targeted by these MIR LEDs.

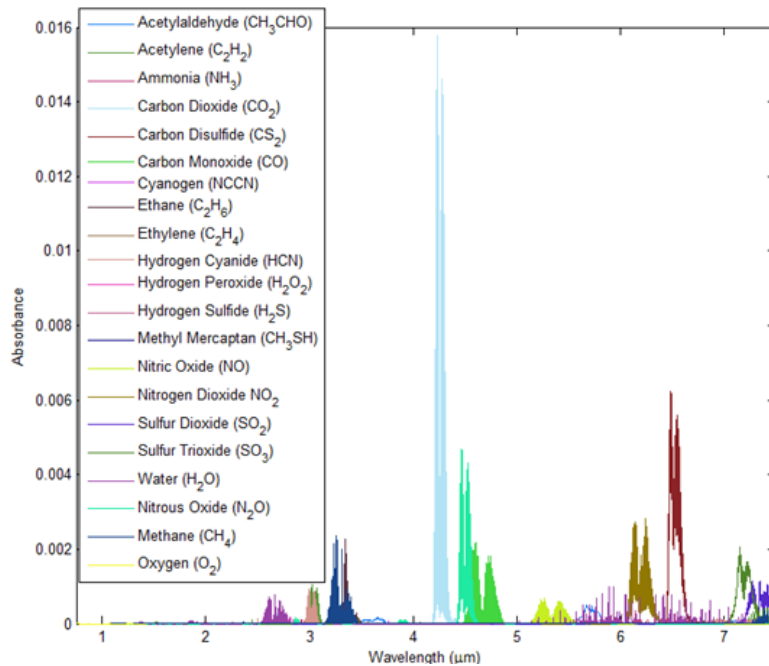


Figure 1: Gases Within the Spectral Region of Available MIR LEDs

1.1 Motivation

This sensor falls under the Federal Aviation Administration Center of Excellence Commercial Space Transportation (FAA COE CST) Research Areas 3.3 and 3.4 in regards to the ECLSS as well as emergency conditions [1]. With the increasing likelihood that space tourism will develop into a viable industry, the number of launches into space will increase. The FAA and the pioneers in the space tourism industry have expressed an interest in a durable, sensitive sensor that is cost-effective and has low power consumption. Before space tourism can begin bringing crews and consumers into space, the FAA must be assured that all safety standards are met, including the fire detection and suppression systems.

1.2 Principles of Operation

Absorption spectroscopy can target a molecular species by its characteristic absorption spectrum. In species concentration measurement, a collimated beam of light with a wavelength characteristic to the targeted species is directed through a gas. The attenuation of the beam is measured by comparing the incident and transmitted radiation, which is related to molecular concentration. Absorption spectroscopy follows from the Beer-Lambert Law (Equation 1) which relates the transmitted intensity I to the incident intensity I_0 when a spectrally narrow radiation at frequency $\nu[\text{cm}^{-1}]$ is directed through a gas medium:

$$T_\nu = \left(\frac{I}{I_0}\right) = \exp(-S\phi Px_i L), \quad (1)$$

Here T_ν is the transmissivity, $S(\text{cm}^{-2} \text{atm}^{-1})$ is the line strength, $\phi(\text{cm})$ the line-shape function, $P(\text{atm})$ is the total pressure, $L(\text{cm})$ the line path length through the gas, and x_i the mole fraction of the absorbing species. The product $k_\nu = S\phi Px_i$ is known as the spectral absorption coefficient. The line strength was generated using the HITRAN 2012 database, which provides a compilation of spectroscopic parameters used to predict and simulate the transmission of light in the atmosphere [2].

1.3 Payload Description

The instrument to be flown was originally developed by the team lead, Kyle Thurmond, as a senior design project in 2013; it was developed in labs at UCF and ORNL and has been evaluated for performance and calibrations [3]. An early version of this sensor is shown in Figure 2 below. The sensor utilizes three LEDs, one centered at $3.6\mu\text{m}$ to serve as a reference (I_0 in Beer's Law), one centered at $4.2\mu\text{m}$ for measuring CO_2 , and one centered at $4.7\mu\text{m}$ for measuring CO . The three LEDs are individually spectrally filtered and spatially collimated; they are then combined into a single beam to be transmitted through the gas under investigation. After being transmitted through the gas, the beam is focused onto a single detector. Each LED's amplitude is modulated at a different frequency so that the signals can be separated via Fourier transform. With this information and a variation of Beer's Law, the concentrations of CO and CO_2 can be derived.

Neat gas calibration measurements were made in an 8cm long line-of-sight calibration cell in order to obtain calibration curves and determine the sensitivity of the sensor to CO₂ and CO [3]. Simultaneous measurements of CO and CO₂ were also completed so as to characterize possible cross-interferences between the species. Additionally, time resolution measurements were performed to demonstrate sensor speed and determine the fastest transients that the sensor can resolve. The sensor was evaluated to have a detectability limit of 30ppm for CO₂ and 400ppm for CO, with no observed cross-interference. The signal is well resolved for fluctuations up to 250Hz. The detectivity limit for CO is being improved so that 10ppm levels are possible by increasing the power to the LEDs and using a multipass cell to increase the path length.

The payload consists of an aluminum box with the sensor mounted to the exterior. The aluminum box is constructed of 0.05in. aluminum sheet and fortified with 1x1in. hollow aluminum construction tubing. A CAD model of the skeletal frame of the aluminum box is shown below in Figure 3. This figure also shows the cRIO DAQ mounted inside the frame and a panel where the sensors driving electronics and power control circuitry will be mounted. The bottom of the frame contains a series of holes that will continue through the aluminum box and will be used to secure the package to the HASP. The box contains the driving electronics and a National Instruments cRIO DAQ, which is necessary to operate the experiment in flight as it will be used for data logging and experiment control. This DAQ was chosen to allow for multiple sensor inputs (photodetector, thermocouples, barometer, etc.) and analog output for controlling LED function output. The sensor and balloon package were also tested in a simulated environment in order to reduce the likeliness of failure during the actual flight. An environmental chamber that can produce conditions close those encountered at 36km, -20°C, and 13mbar was used to test the system.

Once the payload has been powered up, it will begin its normal operations and continue to do so through the duration of the flight. A gas cell will have been loaded into the payload pre-charged with a known gas mixture (N₂/CO₂/CO). This cell will have a membrane so that it is always at atmospheric pressure. Once the power is supplied, the sensor will take a measurement of this cell at some predetermined interval. The data will be stored onboard and accessed post-flight. No serial uplink/downlink or discrete commands will be utilized.

1.4 Scientific Objectives

The primary objectives for this flight are to record simultaneous measurements of CO and CO₂ at the peak altitude and to demonstrate autonomous operations of the sensor in a near-space environment. Intermediate altitude measurements will also be acquired during the flight. The sensor will load a gas cell filled with 89.51% N₂, 4.97% CO, and 5.52% CO₂ which will adjust to the ambient pressure through a diaphragm. Success will be defined by successful resolution of CO₂ and CO at peak altitude, maintaining optical alignment, and proper thermal management of the sensor system. The balloon flight will provide a smoother flight than other options, but vibrations and small g-loads must still be anticipated. A minor misalignment of the optical train could greatly reduce performance or break the sensor. The most critical test will be thermal management of the sensor. The components of the sensor are temperature-controlled through the TECs, which can either cool or heat as needed.

Chapter 2: Team Structure and Management

2.1 Team Demographics

The development of the sensor package was initially led by graduate student Kyle Thurmond, who was assisted by graduate students Justin Urso and Michael Villar and undergraduate student Akshita Parupalli. Mr. Thurmond’s responsibilities included team management, monthly report submissions, and teleconferences. His duties also included programming the instrument’s DAQ, experiment design, and execution. Mr. Urso took on the role of structure engineer, which included the responsibility of readying the hardware for flight. Mr. Villar assumed the role of components engineer, which has the responsibilities of components selections and design. Mr. Urso also was responsible for ensuring that the optics will remain properly aligned during the duration of the flight and that the package can withstand 10g vertical and 5g horizontal shocks. Mr. Villar handled payload driving electronics, support sensors, and interfacing with the HASP. Once Mr. Thurmond graduated, Mr. Villar took over as the project manager and continued with the structural redesign in order to prepare for the balloon flight with the help of Justin Urso and Akshita Parupalli.

Dr. Subith Vasu is the University of Central Florida faculty advisor for the team and has extensive knowledge of spectroscopic sensors. Dr. Bill Partridge is a distinguished research staff member at Oak Ridge National Laboratory (ORNL) who has been provided valued expertise since the project was started. Funding is provided by Federal Aviation Administration, under the Center of Excellence Commercial Space Transportation (FAA COE CST).

Table 1: Team Personnel, Roles, and Contact Information

Project Manager	Kyle Thurmond Graduate Student	Gender: Male Ethnicity: non-Hispanic Race: Caucasian/White Student Status: M.S. 2016 (Mechanical Engineering) Disability that limits a life activity: No Current Position: SpaceX, CA	kthurmond@knights.ucf.edu (407)617-0475
Structure Engineer	Justin Urso Graduate Student	Gender: Male Ethnicity: non-Hispanic Race: Caucasian/White Student Status: PhD Disability that limits a life activity: No	justin.urso13@knights.ucf.edu (352)817-9212
Components Engineer	Michael Villar Graduate Student	Gender: Male Ethnicity: non-Hispanic Race: Caucasian/White Student Status: MS	mvillar@knights.ucf.edu (561) 512-3953

		Disability that limits a life activity: No	
Faculty Advisor	Dr. Subith Vasu Principal Investigator		subith@ucf.edu (407)823-3468
Collaborator	Dr. Bill Partridge Jr.		partridgewp@ornl.gov (865)850-8592
Technical Monitor	Nickolas Demidovich		FAA Technical Monitor Nickolas.Demidovich@faa.gov
	Akshita Parupalli Undergraduate Student	Gender: Female Ethnicity: non-Hispanic Race: Asian Student Status: Undergraduate Disability that limits a life activity: No	Akshita.parupalli@kni.ghs.ucf.edu (321)696-9969

2.2 Timeline

Table 3 below shows the expected schedule for the project, with milestones in bold. The payload will be put under testing as soon as possible so that modifications can be made if any issues occur. The cycle of testing and corrective actions will take place through the summer until flight preparation is underway.

Table 2: Work Schedule by Month from January of 2016

Tasks	Month											
	1	2	3	4	5	6	7	8	9	10	11	12
Finalize Hardware Upgrades	X											
Program DAQ	X											
Thermal Management Analysis	X	X										
Complete Calibrations		X										
Environmental Chamber Experiments Rounds		X			X							
Corrective Actions			X	X		X	X					
Preliminary PSIP Document				X								
Final PSIP Document					X							
Flight Preparations								X				
Flight									X			
Reports & Publications										X	X	X

CHAPTER 3: Sensor Design

3.1 Infrared Source

Chapter 1 presented the advantages of using LEDs over the more conventional lasers, though this was more of a discussion on NDIR versus laser absorption spectroscopy (LAS). There are a few low-cost, broad spectrum sources that have similarly appealing features to LEDs. By far, the most commonly used source is the tungsten filament bulb (micro-bulb) as it cheap and has a high output. Another currently emerging technology is thin foil element infrared sources, which work by heating a very thin film of metal (titanium or platinum alloy) to $\sim 1000^{\circ}\text{C}$ then letting it cool through radiation. Currently, micro-bulbs dominate the market for NDIR sensors. While their relatively high output and low cost has afforded them success in the basic consumer market, their limitations of having high drift, low efficiency, low modulation rates, and limited spectral range prevent their adaption to the more specialized markets discussed here. The micro-bulb operates by heating a tungsten filament inside of a glass envelope to temperatures $\sim 3000\text{K}$, which causes the filament to evaporate over time. This causes the output of the bulb to drift significantly which then requires regular calibration of the sensor to offset. The high operating temperature also makes the bulb inefficient compared to the LEDs; this makes it less appealing for low-power jobs. Finally, micro-bulbs are limited to modulation rates of only a few hertz while LEDs can be modulated at rates as high 50MHz. This makes micro-bulbs unappealing for situations demanding high time resolution. Infrared foil elements provide similar magnitude intensity output as micro-bulbs, however they provide greater spectral range and slightly faster modulations rates due to smaller thermal mass [18][15]. They are, however, still limited to no more than $\sim 1\text{kHz}$ modulation rate which makes them ill-suited for EGR measurements which require speeds greater than 10kHz [16]. The selection of MIR LEDs for the source was ultimately determined by their low power consumption (20000hrs) [17]. The LEDs cost is slightly greater than that of the other sources; however, for the applications being considered, the cost is still considerably low. The main drawback of LEDs is their lower output, but this can be accounted for with certain decisions such as longer or folded path lengths.

3.2 Component Selection and Design Details

This sensor utilizes three LEDs to cover three different wavelength regions: a reference LED centered near $3.6\mu\text{m}$, one LED near $4.2\mu\text{m}$ for detecting CO_2 , and one LED near $4.7\mu\text{m}$ for detecting CO. Figure 2 shows the normalized spectral profiles of these LEDs overlaid with the absorption features of CO and CO_2 ; it is clear from Figure 2 that the LEDs are spectrally broader than the individual absorption transitions, and that the associated measurements will be the integral of absorption from many individual lines in the indicated bands. Figure 2 also shows the spectral profiles of source-specific band-pass filters selected to narrow the bandwidth of the LEDs; these reduce spectral overlap between the three LEDs and associated cross interference. The CO_2 filter has good overlap with the CO_2 absorption features, however the CO filter happens to overlap a valley in its absorption features; this hurts its already weak signal. A new filter that provides greater overlap has since been acquired.

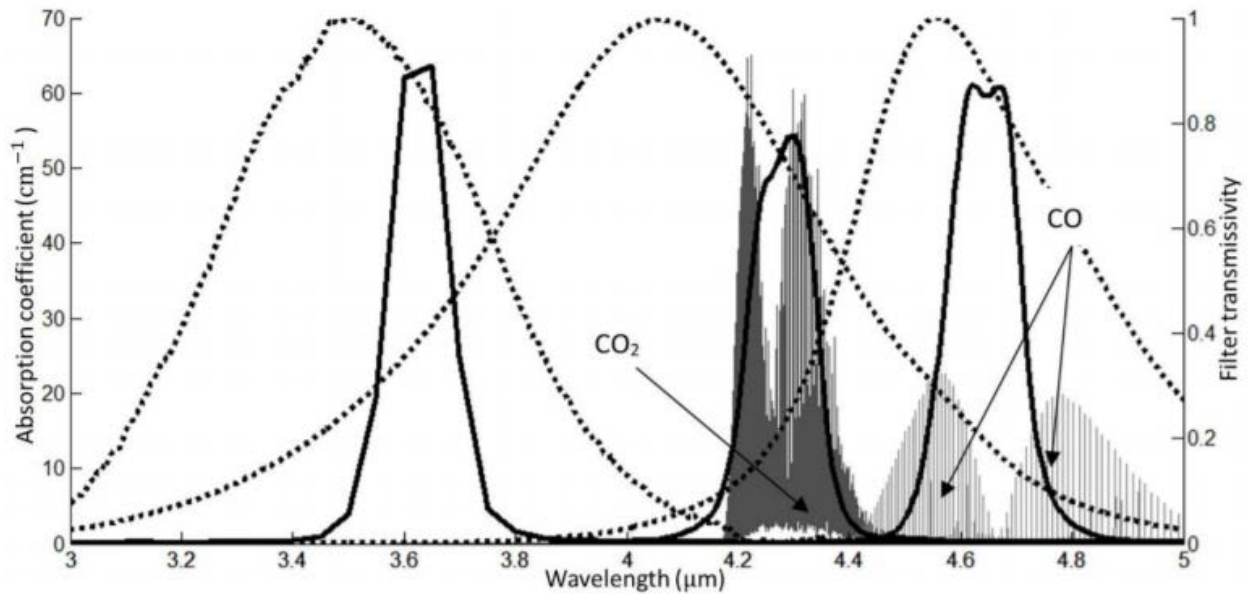


Figure 2: Normalized spectral profiles of the LEDs (dashed lines) and filters (solid lines)

The output of the LEDs (spectrally and in intensity) is dependent on their temperature, so in order to achieve a steadier and more consistent output performance, each LED was individually temperature controlled (to $-10 \pm 0.2^\circ\text{C}$) using a two stage thermal electric cooler (TEC). The temperature dependent spectral characteristics of one of the LEDs ($3.6\mu\text{m}$) is shown in Figure 3 below [18]. For typical room temperature operation, the TECs can be operated to create a temperature difference that cools the LED ($\sim 10^\circ\text{C}$) and rejects heat to a heat sink ($\sim 26^\circ\text{C}$). When operating at lower temperatures expected in various space vehicle environments (-15 to -50°C), the poles on the TECs are switched so that they actively heat the LEDs instead. For this case it may be necessary to supply a thermal pool for the TECs to draw from in order to sufficiently maintain LED temperature [20].

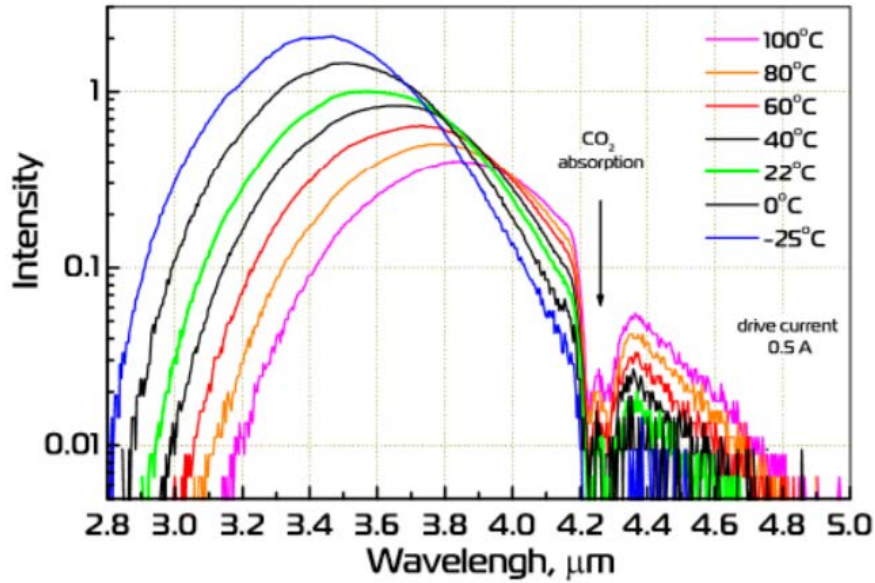


Figure 3 Emission spectral of the 3.6 μm LED at different temperatures

Using a single detector for the three LED signals reduces instrument cost and complexities associate with multiple detectors; e.g., accounting for detector-specific response, dark current, noise and other characteristics. This single-detector approach requires the three LEDs to be combined into a single measurement beam. The LEDs were individually collimated, filtered with the appropriate band-pass filters and combined using two Pellicle beam splitters as shown in Figure 8. The beam splitters have their own spectral characteristics, as shown in Table 3, so the arrangement of the LEDs was optimized so that the 4.7 μm LED, which has lowest intensity output, lost the least amount of signal; the 4.2 μm was optimized second [21]. The output of each LED was modulated at a unique frequency by a dedicated function generator or DAQ unit using a square-wave unity duty-cycle function; i.e., the 3.6 μm , 4.2 μm and, 4.7 μm LEDs were modulated at 55, 77 and 115 kHz, respectively. The signal corresponding to each LED was determined from the Fourier transform of the combined single-detector signal as that at the corresponding modulation frequency. A Vigo Systems three-stage TEC photovoltaic detector (model PVI-3TE-5, Boston Electronics) with an STCC-04 TEC controller (from the same manufacturer and source) was used. This detector has fast response and high sensitivity to radiation between 3 and 5 μm .

Table 3: Pellicle Beam Splitter Transmittance/Reflectance

LED Center Wavelength (μm)	Reflectance (%)	Transmittance (%)
3.6	33	67
4.2	45	55
4.7	48	53

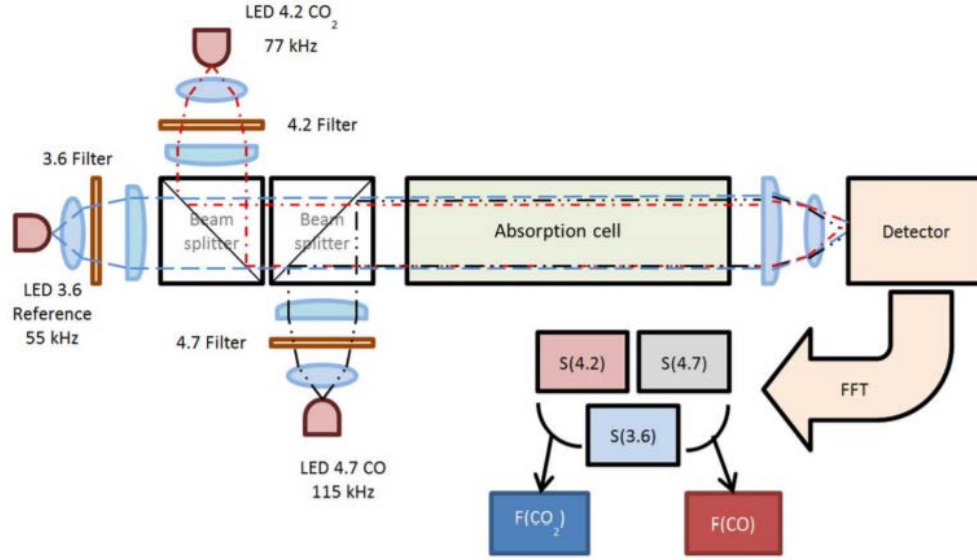


Figure 4: Sensor hardware and processing schematic, including measurement flow cell

The catch is simply the detector and lenses to focus the beam from the light guide into detector. The detector selected is a Vigo Systems three-stage-thermoelectrically-cooled (TEC) photovoltaic detector (model PVI-3TE-5). An STCC-04 TEC controller from the same manufacturer is used detector temperature control. Further specifications for these instruments can be found in appendix. The detectability D^* of the detector is defined as:

$$D^* \equiv \frac{\sqrt{A \times \Delta f}}{NEP} = R_v \frac{\sqrt{A \times \Delta f}}{V_n},$$

where A is the detector area in cm^2 , Δf is the signal bandwidth, V_n is noise voltage, R_v is the voltage responsivity of the detector, and NEP is the Noise Equivalent Power [19]. NEP is the optical input power to the detector that produces a signal-to-noise ratio of unity ($S/N = 1$). For this detector, $A = 0.01 \text{ cm}^2$ and $D^* = 1011$. The optical signal at the intermediate frequency due to optical power P and power of radiation of local oscillator PL is $VI = R_v (2PPL)^{1/2}$. NEP is the optical power that is generated to make the signal equal to noise voltage V_n , so

$$NEP = \frac{V_n^2}{2P_L R_v^2},$$

Solving for R_v in equation 6 and substituting into equation 7:

$$NEP = \frac{A \Delta f}{2P_L D^{*2}},$$

The lowest expected LED power output (from the $4.7\mu\text{m}$ LED) is around 2.5×10^{-7} W. For a bandwidth of 79 kHz, $NEP = 1.5 \times 10^{-13}$ W. An optical power output greater than 1.5×10^{-13} W is necessary to be distinguishable from noise, which is sufficient for the selected LEDs.

3.3 Optical Train Optimization and Simulations

In order to optimize sensor performance, the spatially extended incoherent LED emission must be carefully coupled into and within the system. Optical-design software (Radiant ZEMAX) allowed simulation of the entire sensor optical system and was used to optimize the optical configuration [20]. The software shows that multiple collimating lenses and focusing lenses would be required in order to acquire an acceptably collimated beam that is focused to a sufficiently small point for minimal losses. First, the single-lens design is compared with the multi-lens design, and the optimal lens configuration as well as estimated signal losses are presented. The sensor utilizes three LEDs, which must combine into a single beam. Each LED must be collimated, combined with the other lights, and then focused to a point; each LED has different collimated beam pathlengths depending on how many beam splitters it must pass through. This has been a vital part of the designing processes given the inherent difficulties in focusing an incoherent source such as an LED to a point; a significant amount of power can be lost when attempting to focus the light to small point such as a $1 \times 1\text{mm}$ square for the case of this detector. Figures 5 and 6 below show a one collimating lens and one launch lens setup vs. a two collimating lens and two launch lens approach for the pitch setup. In these simulations, the LEDs are focused into a hollow waveguide (HWG) with an inner bore of 1mm. The detector face is placed at the immediate end of the HWG, so the results shown are effectively what would be captured by the HWG. It is clearly seen that with the second design, a much more collimated beam is achieved, which results in less power loss as the light is transmitted through the beam splitters and combined with the other LEDs. The squares here show the irradiance on the detector face. Each square is 6mm by 6mm, however only the light within the 1mm inner bore of the HWG will reach the detector face. Notice that, with the second design, the beam was focused to a smaller and more power dense point. With a 1mm inner bore diameter for the HWG, most of the signal is being lost at the entrance of the light guides; therefore, the smaller point is desired. The efficiency at the HWG entranced increased from 84% for design one to 98% for design two.

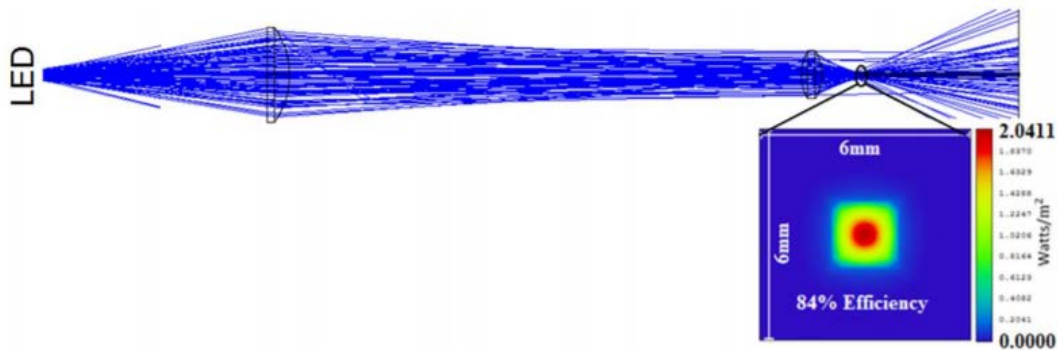


Figure 5: Pitch lens design one

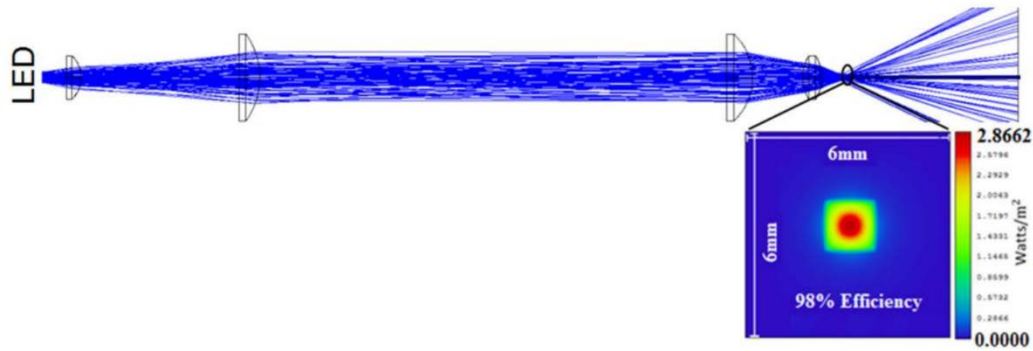


Figure 6: Pitch lens design two

Figure 7 shows a simulation of the $3.6\mu\text{m}$ LED as it is nominally collimated, transmitted through the beam-combining optics and measurement cell, and focused onto the detector; this reflects the design configuration implemented in these studies. The LED beams were nominally collimated to minimize signal loss from vignetting or clipping by hardware surfaces during its travel through the sensor system; two plano-convex lenses (20mm and 50mm focal length CaF₂ lenses from Thorlabs) produced a semi-collimated beam with a working diameter (i.e., between the collimating and focusing lens sets) of ca. 12.7mm. Following transmission through the measurement cell, a plano-convex lens coupled with a bi-convex lens (40mm and 15mm focal length CaF₂ lenses, respectively) was used to focus the combined three LED beams onto the 1-mm² square detector; i.e., although each LED has a dedicated collimating lens set, they have a common focusing lens set as indicated in Figure 4.

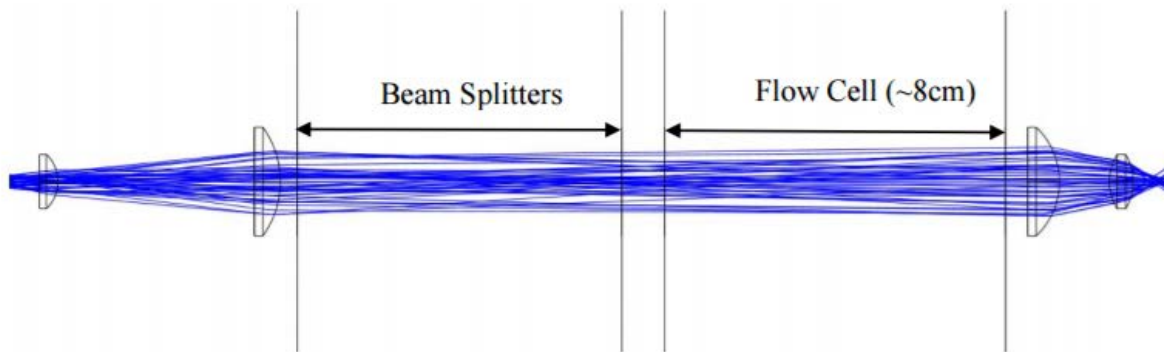


Figure 7: Simulation of the entire beam path for the $3.6\mu\text{m}$ LED emission

Figure 7 shows the simulation detector face for this configuration with a 1x1mm surface, the same dimensions as the Vigo Systems detector. The simulations suggest that an optical efficiency of 45% may be possible with this configuration, though this does not include losses from beam splitters, bandpass filters, windows, or atmospheric gas absorption. In total, approximately less than 1/3 of the LED emission is captured by the detector, reflecting the challenge of collimating and focusing the emission of spatially extended incoherent sources to a

small area. Even with these significant losses, significant instrument performance is possible. Future work will focus on optimizing the optics, with the potential of doubling the signal and realizing corresponding diagnostic benefits regarding signal-to-noise ratio, temporal resolution, and detection limit.

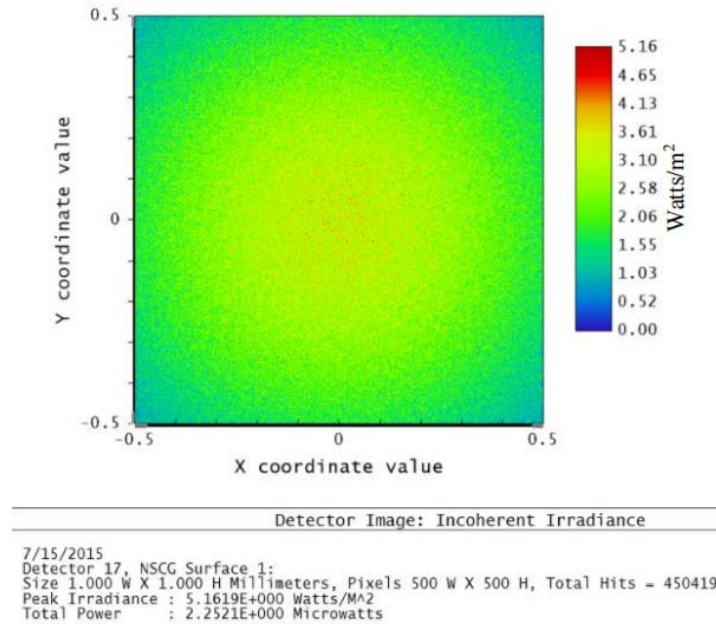


Figure 8: Simulation detector face

3.4 Driving Electronics

Original testing of this sensor started by using function generators to drive the LEDs, however these did not seem to supply a sufficient amount of current. Driving the LEDs at max specifications (pulsed power) requires $\sim 0.45\text{V}$ at $\sim 1\text{A}$. To meet the current demands of the LEDs, Wavelength Electronics WLD3343 general purpose drivers were acquired. These were eventually adopted to drive the TECs for the LEDs as well. In Figure 9 below, the output from the LEDs while driven from the function vs. those driven by the WLD3342 modules is compared. The top image shows the LEDs driven with the SRS DS345 function generator while the bottom image shows the LEDs driven with the WLD3343 driver modules. Note that each LED was modulated at a different frequency in these test sets, however all else was equal. The output the $3.6\mu\text{m}$ LED was increased by 78.9 times, the $4.2\mu\text{m}$ LED was increased by 13.5 times, and the $4.7\mu\text{m}$ was increased by 6.1 times.

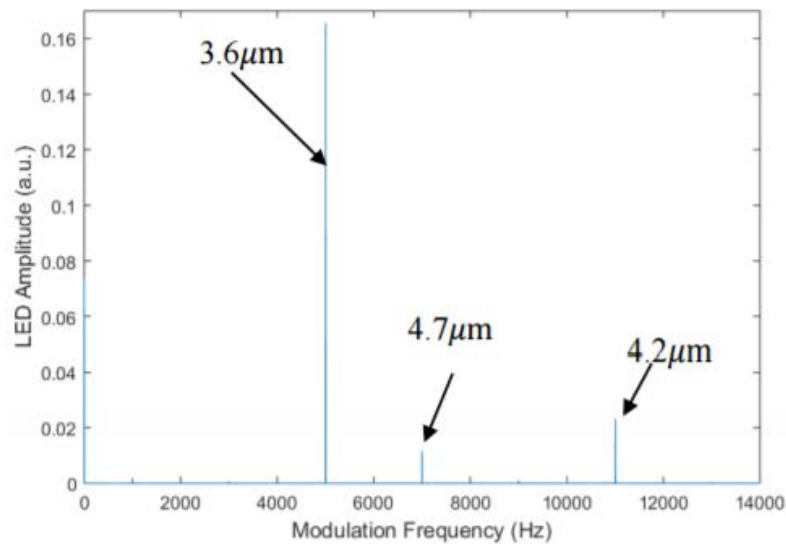
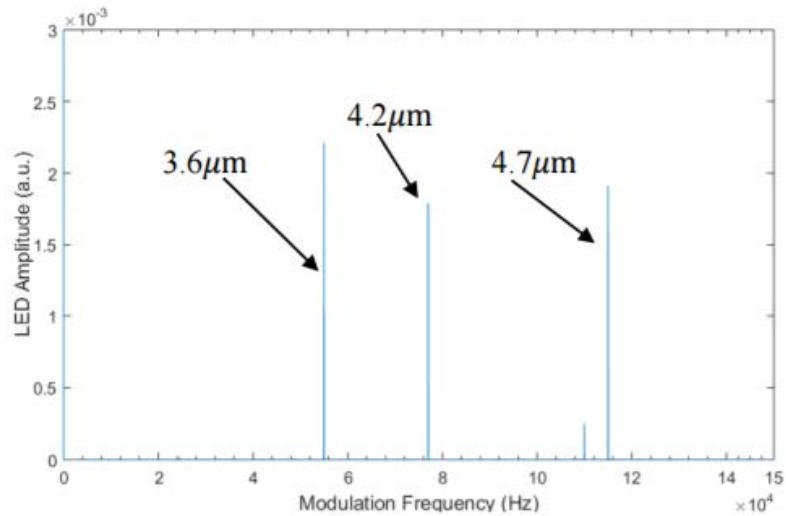


Figure 9: LED output comparison for upgraded circuit

The WLD3342 modules serve to properly drive the LEDs properly as well as power them using batteries, which is will be critical on the high altitude balloon flight. However, there have been a few drawbacks that have been observed. First, their output appears to be proportional to their power source voltage supply, so if they are being powered by batteries, their current output with decline steadily as the batteries supply is drained. This is particularly an issue because they are also very inefficient. They produce significant amounts of heat and thus are a large load on the battery cells. Furthermore, this heat can build up if it is not sufficiently dissipated causing the modules to overheat. Future iterations should consider more efficient current regulators.

3.5 Thermal Management

While this sensor is designed to operate in multiple environments, the greatest challenges in thermal management is operation in low pressures as heat rejection is greatly reduced due to low heat convection efficacy. As previously mentioned, the LEDs and detector are equipped with TECs which can be used to cool or heat the component. For the detector, we are only interested in cooling since its operating temperature is below all environmental temperatures being considered (detector operating temperature is -60°C). The LEDs and detector are very small masses and require very little to maintain their temperature. A small aluminum mass is used as a thermal pool for the LEDs in both standard and low pressure conditions, which is shown below in Figure 14. Since the TEC are only turned on for very brief periods of time, the thermal masses are able to dissipate or absorb heat as needed at a sufficient rate. This setup is validated and discussed in Chapter 4.

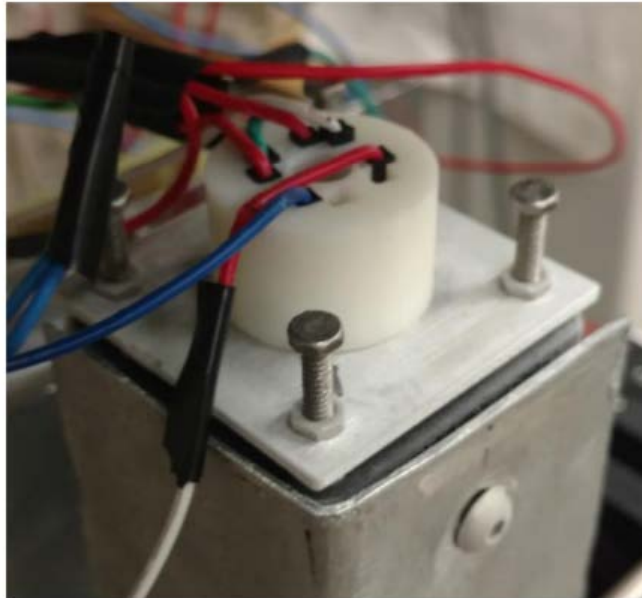


Figure 10: The aluminum mass for the $3.6\mu\text{m}$ LED

3.6 DAQ Control

A National Instruments cRIO-9031 DAQ is used for data acquisition and to control the sensor and its components. This was selected as it is a self-contained and robust DAQ system which allows for battery operation in the varied environments where testing is planned. Specific tasks of the DAQ include: detector data logging, LED signal function generation, and LED temperature control. All of these tasks can be performed autonomously, or without any intervention from a user. Figure 11 below shows the architecture of the DAQ's code or virtual instruments (VIs).

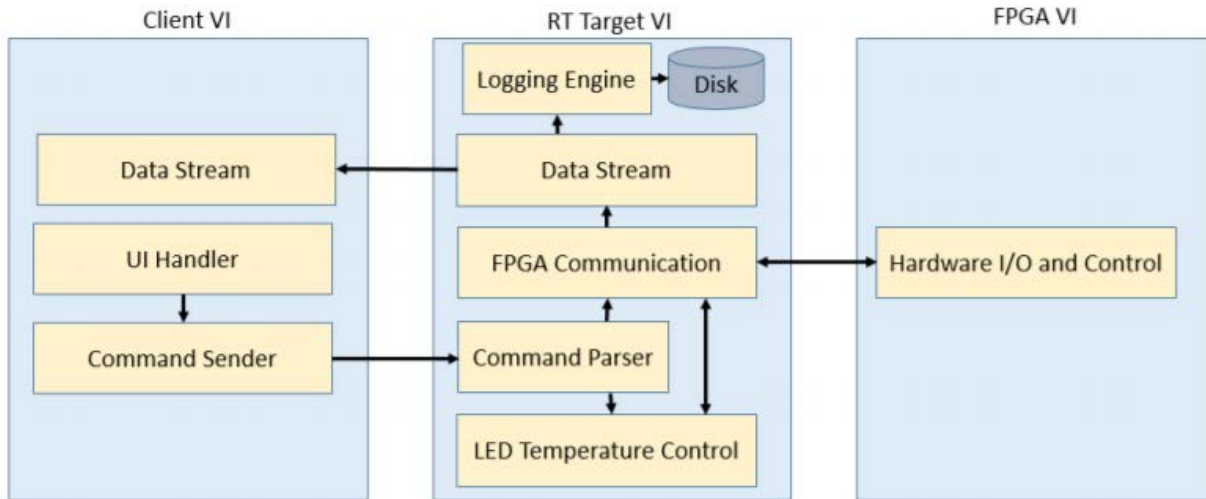


Figure 11: Schematic depicting the sensor DAQ architecture

There are three VIs: one runs on the DAQ's field programmable gate array (FPGA), one runs on the DAQ's real-time host CPU, and one runs on the user's computer. The last VI is optional; it is not necessary for the operation of the sensor and is only used for real time diagnostics and control. It allows a user to view various graphs related to the sensors performance so that they may make adjustments for its optimal operation. If no computer is attached to the DAQ, this VI does not run. The FPGA VI is a highly efficient code that has a sole purpose of controlling input and output from the DAQ. All data handling and manipulation is handled on the DAQ's host CPU and the RT Target VI. The main tasks here include FPGA communication, data logging, and temperature controls for the LEDs. While client operated, the user can save data at a specified length of time and append a comment to the data file. When operating headless, the DAQ will save data at a specified time interval with the last set settings. For the temperature controls of the LEDs, a simple on/off control loop is used since the LEDs have such low mass. This was able to maintain 32 the LEDs temperatures within $\pm 0.2^{\circ}\text{C}$. The poles for each LED TEC were switch using relays which were controlled using digital IO from the DAQ. The greatest challenge with programming the DAQ was streaming the detector signal from FPGA to the host CPU, then creating a lossless buffer of the data that was ready for when the client was ready to save the data. The DAQ samples the detector at 100kS/sec which is streamed from the FPGA to the host CPU with a direct memory access (DMA) first in first out (FIFO) data stream. On the host CPU end a circular buffer is created that is two times greater than the save duration (usually one second). When a save is made, data is allowed to be lost during the save process. The DAQ code (VIs) are in Appendix.

3.7 Power Specifications

Figure 12 below shows the general interface between the power source provided by HASP and the sensor payload. HASP provides approximately +30 VD that will be down-regulated to +24 VDC to power the DAQ. This is then further regulated down to +12 VDC to power the LED and TEC electronics boards along with the detector board. Figure 13 below shows the overall circuit

schematic for LED and TEC control. The +12 VDC powers the LEDs and TECs directly. LED and TEC signal control is powered and modulated by a regulated +5 VDC line from the NI-cRIO DAQ. Table 4 shows the power draw breakdown per component as well as the total maximum power consumption of the payload.

Table 4: Power Breakdown

Component	Voltage	Current	Power	Note
Detector	5V	1.1A (2 stage TEC) or .43A (3Stage)	5.5W	Max, including TEC operation
LED	0.45V	900mA	0.405W	Per LED, no TEC operation
TEC on LED	2.78V	1A	2.78W	Per embedded TEC, max conditions
Driving Electronics	12V	1.67A	24W	Max draw, full operation
cRIO-9031	12V	.8A	10W	Max draw, full operation
Overall System	24V	2.05A	49.055W	Draw of entire system from Power Supply

Table 5: Power Breakdown for HASP System

Component	Quantity	Unit Power, W	Total Comp Power, W
Detector	1	5.5	5.5W
LED	3	.405	1.215W
TEC for LED	3	2.78	8.34W
Driving Elec.	1	24	24W
cRIO-9031	1	10	10W
		Total:	49.055W

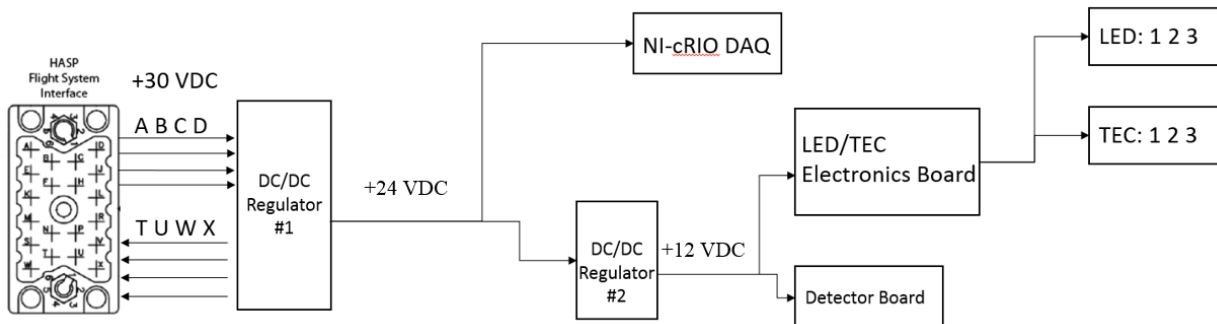


Figure 12: HASP EDAC516 connector interface with Sensor payload power system

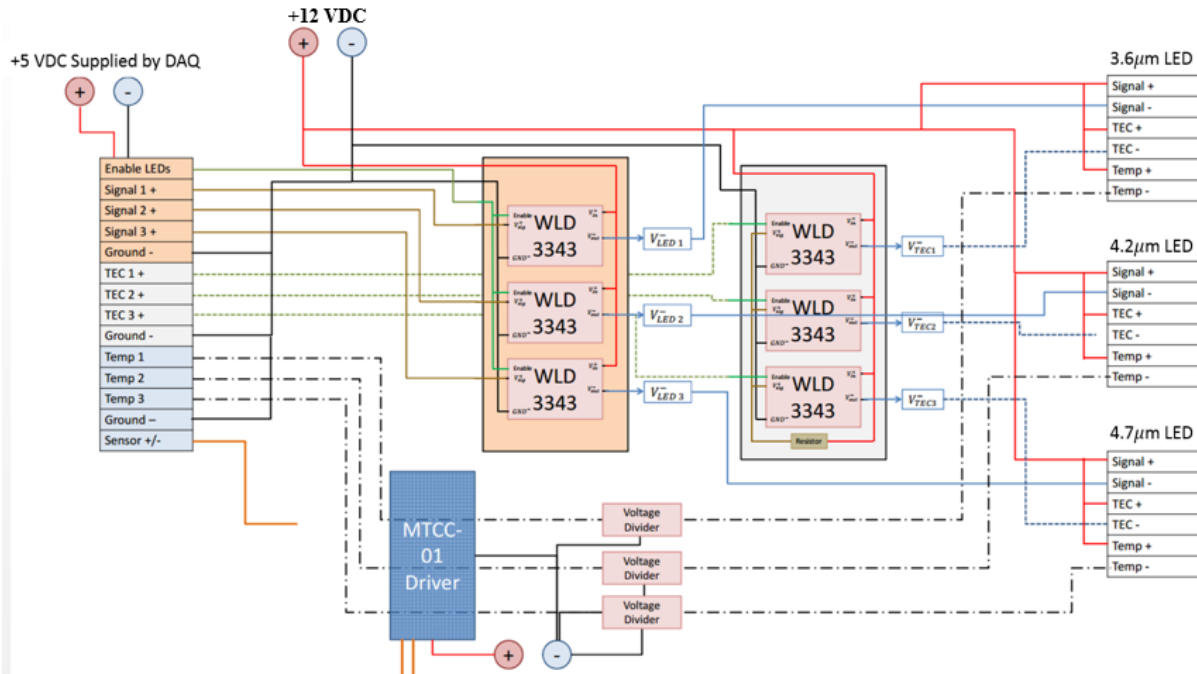


Figure 13: LED/TEC Electronics Board as shown in Power Schematic of Figure 12

Table 6: Other Relevant Power Information

DC/DC Regulator	Manufacturer	Input Voltage	Output Voltage	Max Power Output
CBS3502424-RT	Cosel	20-36 V	24 V	> 350 W
CBS3502412	Cosel	18-36 V	12 V	> 350 W

3.8 Overall HASP Flight Design

The weight of the payload as of 4/24/2016 is shown in Table 7 below. The total weight is 8 ± 1.243 kg with uncertainty due to unfinished structural hardware. The LEDs, detector, optics, DAQ, and driving electronics are all weighed directly, while the structure is estimated by calculations using SolidWorks models. Figures 14, 15, and 16 below show the SolidWorks model of the system.

Table 7: Payload Weight

Component	Mass (g)	Mass Uncertainty (g)
LED + TEC x3	30	3
Detector + TEC	100	5
Optics	100	20
Structure	5260	1000
DAQ	2400	200
Driving Electronics	110	15
Total	8000	1243

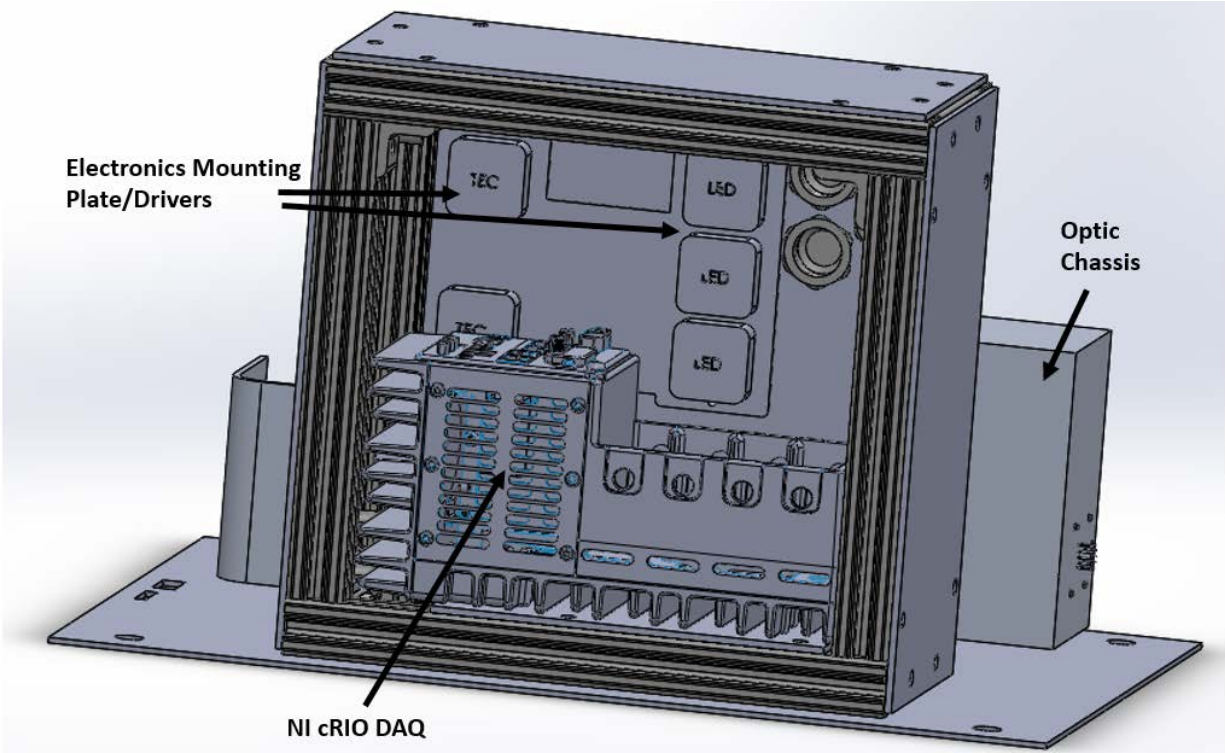


Figure 14: Payload attached to HASP Mechanical Interface Plate

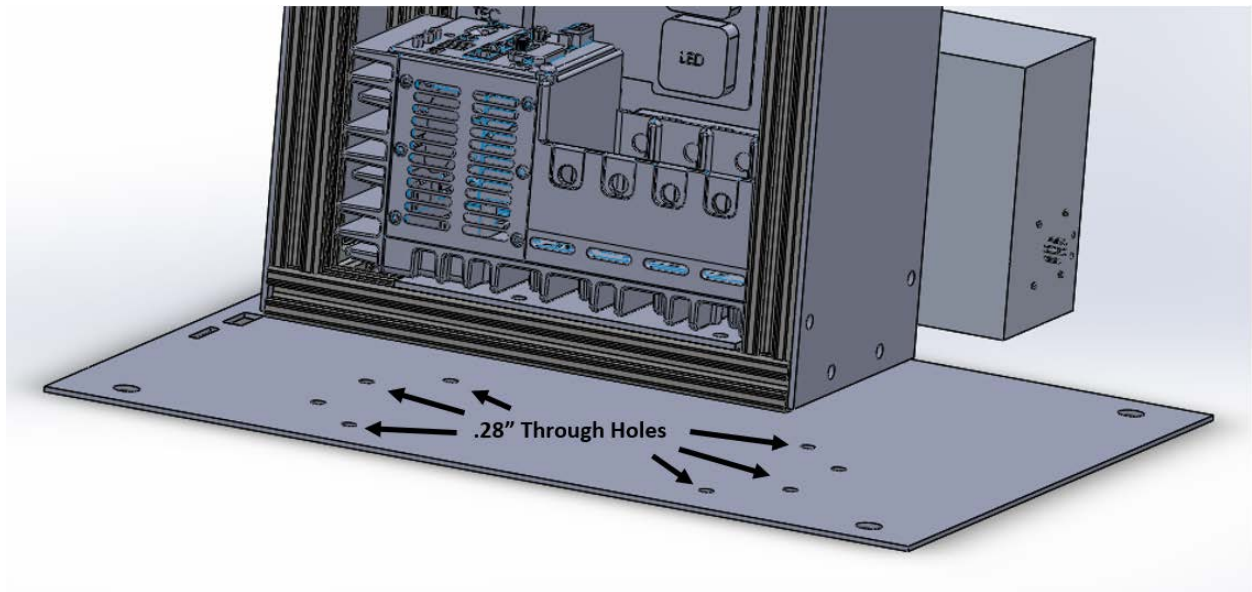


Figure 15: Payload attachment locations on HASP Mechanical Interface Plate

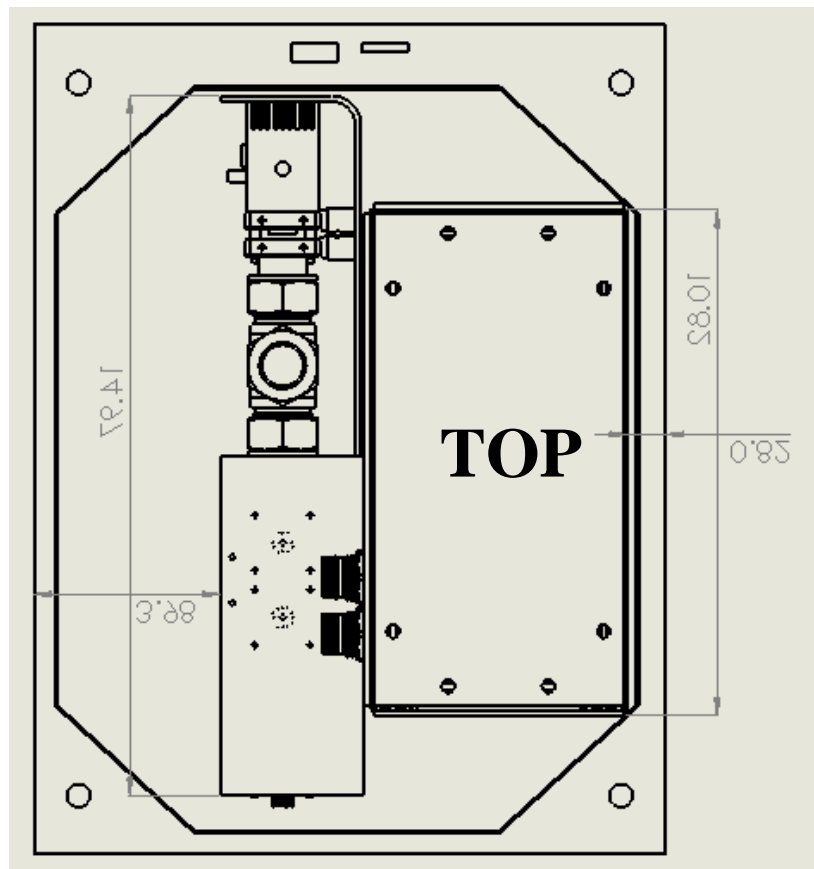


Figure 16: Top view of payload on HASP Mechanical Interface Plate (units are in inches)

The test cell depicted was filled with a gas mixture of 89.51% N₂, 4.97% CO, and 5.52% CO₂. The test cell's volume is 1.7948 in³, and it was filled to 1atm at the ground. This minute amount of CO was deemed to not pose a hazard to HASP or the ground crew. The cell contains a built-in diaphragm that keeps internal cell pressure equal to ambient pressure. This allowed for varying pressure measurements throughout the duration of the flight while removing the issue of having a pressurized cell at the flight altitudes. Figure 17 below shows the finalized system that was prepared for the balloon flight.

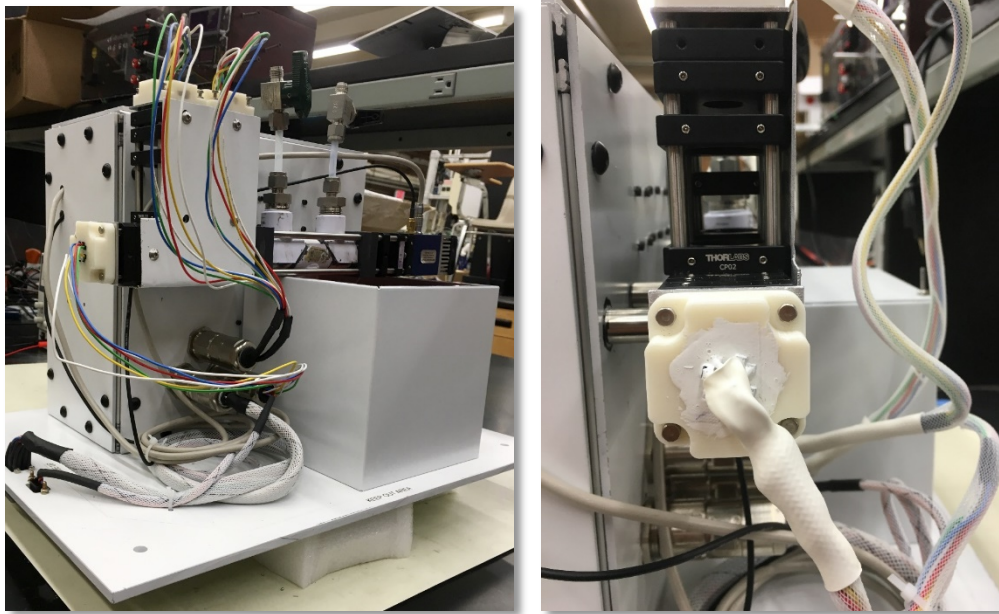


Figure 17: Pictures of the built system displaying the LED setup

CHAPTER 4: Validation Tests

4.1 Experiment Apparatuses

For validation and calibration of the absorption sensor, a simple flow cell was constructed out of PVC pipe that is shown in Figure 18 below. The cell simply functions to allow the flow of gases while also giving optical access. Gas flow access given by the two dark gray perpendicular PVC tubes while optical access runs parallel to the flow. The white section is essentially two PVC tees with sapphire windows glued in one end, gas access in the perpendicular port, and the other end is connected by a nylon tube that is secured with a hose clamp. This allows the length of the cell to be increased. The minimum length is 7.97cm which is the length throughout this study. This cell also has a solenoid valve equipped to it which was intended for time-resolution study how this was never used and instead a different approach was taken.



Figure 18: Simple flow cell constructed of PVC, nylon tubing, and sapphire windows

4.2 Detectability Limit, Cross Interference, and Simultaneous Measurements

The sensor performance was evaluated using neat gas mixtures to quantify species response factors, noise and detection limits, and cross interferences. The flowing measurement cell (cf. Absorption Cell in Figure 17) was constructed from PVC tubing, had sapphire windows, an 8-cm long absorption path length, and tubing connectors on each end to allow flow of the measurement gases. During evaluation and applications, the sensor was placed in an N₂-purged enclosure to eliminate ambient CO and CO₂ from the free-space optical train, and errors due to additional light absorption outside the measurement cell. Neat bottled gas standards and a ten-point gas divider (STEC SGD-710C) were used to control the measurement gas composition; the standards included 1% CO₂, 10% CO₂ and 4% CO, all in N₂ balance. A secondary rotameter pair was used for some of the cross-sensitivity studies. Single-gas calibration curves were measured by diluting the standards with ultra-high purity nitrogen; CO₂ was stepped from 0% to 1% in 0.1% intervals, and

from 0% to 10% in 1% intervals, and CO was stepped from 0% to 4% in 0.4% intervals. Two methods were used to evaluate cross-interference between CO₂ and CO. In the first method, the primary standard was varied as described for the single-gas calibrations, using the gas divider and N₂ diluent, and combined with an N₂-diluted mixture of the secondary standard using the rotameter pair; i.e., when CO₂ was the primary standard, CO was the secondary and vice-a-versa, and the concentration of the secondary standard remained constant throughout all of the measurements. In the second method, the CO₂ and CO mirrored each other between zero and span levels by using the gas divider with CO used as the ‘standard,’ and CO₂ as the diluent; e.g., as CO₂ was stepped from 0-10% while CO was stepped from 4-0%. Two measurements were taken at each gas composition setting: one while stepping up the concentration of the standard and one while stepping down; lack of hysteresis between the two data sets confirmed that the cell reach steady state at each composition element of the calibration scan. The CO₂ and CO calibration curves from the single-gas measurements are shown in Figure 20, along with the 2-sigma (95.4% confidence interval) standard deviation curves. The measurements exhibited low variation between experiments. The non-linear calibration curves are typical of broadband multi-feature absorption⁹, and deviate from the linear response that would be typical of narrow-band (e.g., laser-based) absorption. Although in future work we plan to develop calibrations based on broadband absorption theory, the Figure 19 curves can be used parametrically to convert sensor output to absolute CO₂ and CO concentration levels. The single gas detection limits, defined as the concentration where the signal-to-noise ratio (SNR) is unity (signal = 2-sigma), were determined to be 30ppm CO₂ and 400ppm CO using the 8-cm long measurement cell; changes in the absorption pathlength would inversely scale these detection limit values. Although the intrinsic and secondary (e.g., induced by function generators, etc.) noise was similar for the 4.2μm (CO₂) and 4.7μm (CO) LEDs, the 4.2μm LED had ca. twice the emission power. Thus, the CO₂ measurements have correspondingly lower SNR, and lower detection limit; since signal is also influenced by spectral and LED parameters in relation to the sensitivity discussion below, the detection limit gain (i.e., 30 vs. 400 ppm) is much greater than the power difference between the two LEDs.

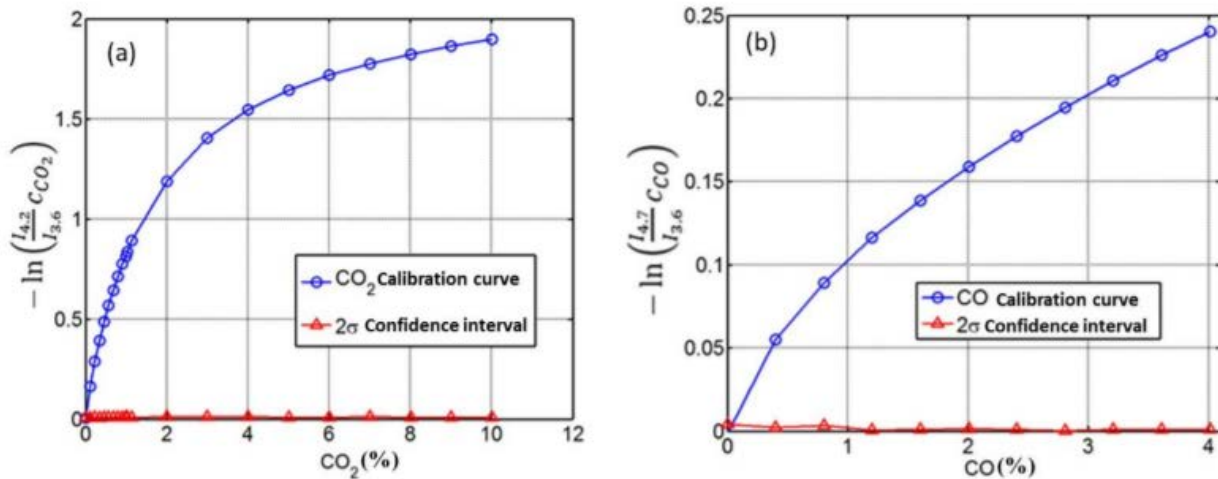


Figure 19: Calibration results for (a) CO₂ and (b) CO in the 8cm calibration cell

The measurement sensitivity is indicated by the local slope of the calibration curves as shown in Figure 20, which indicates the sensor is more sensitive to CO₂ than CO throughout the CO calibration range. The difference in sensitivity and detection limit between the two gases is attributed to the probed spectral absorption features and LED-filter nature. As shown in Figure 6, the CO₂ absorption features are much stronger than those of CO, and the spectra and LED-filter bandwidth are such that a greater number of CO₂ absorption features are measured compared to CO. This causes the sensor's CO₂ sensitivity to be greater than that for CO. Figure 6 shows that many long-wavelength CO transitions within the 4.7 μ m-LED emission were rejected by the bandpass filter; the CO sensitivity could be correspondingly improved by using a different filter which incorporated these additional transitions into the CO measurement. For typical narrow-band absorption the sensitivity would be approximately constant and would be proportional to the spectral absorption coefficient of the targeted transition. The decreasing sensitivity with increasing concentration is due to the stronger transitions becoming saturated; as saturation progresses, the 40 specific absorption changes per unit concentration change goes to zero, resulting in the continuously degraded sensitivity. In contrast to the CO₂ behavior in Figure 21, the sensor's CO sensitivity is nearly constant above ca. 1.5%, which is consistent with the measurement being based on weaker absorption features and specifically fewer lines in the saturation regime.

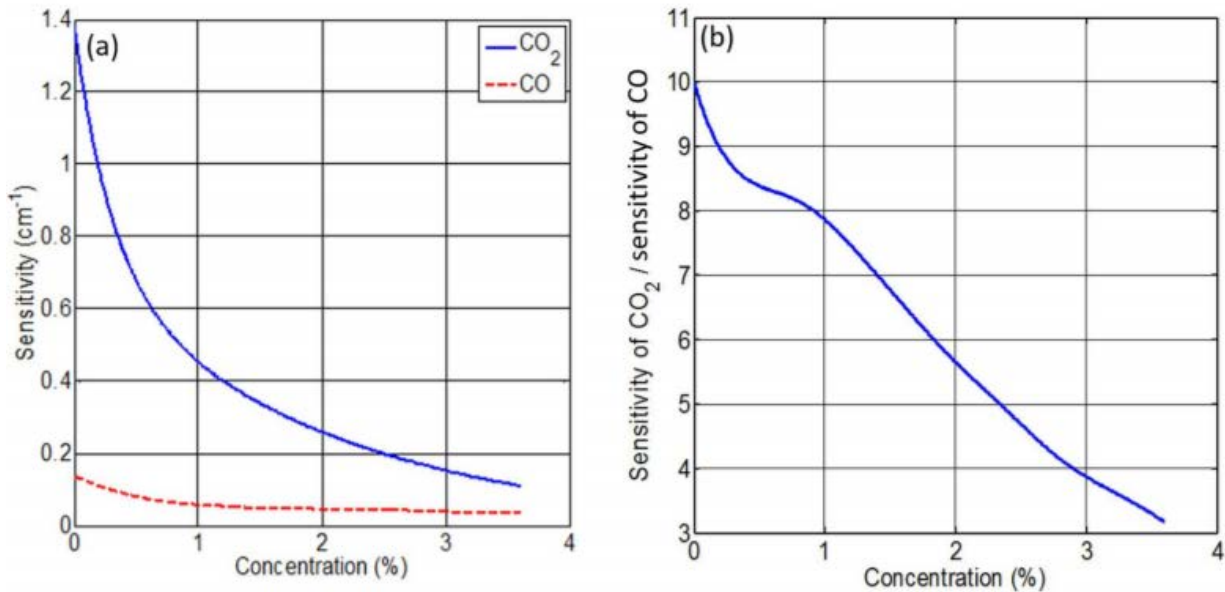


Figure 20: Sensitivity analysis based on the local slope of the calibration curves

Figure 21 highlights the lack of cross interferences between the CO₂ and CO measurements, by overlaying the single-gas calibration curves with those from the stepped and constant cross-interference measurements. The single-gas calibration curves (Figure 19 data) are plotted as lines, while results from the constant and stepped interference experiments are indicated as circle and crosses, respectively. The error bar for the data points are smaller than the symbols used in the plot. Any cross-interference between CO₂ and CO would cause the observed signals for each to diverge from the single-gas calibration results. However, Figure 21 indicates excellent

agreement between the various calibration results, and no practical cross-interference for either CO₂ or CO.

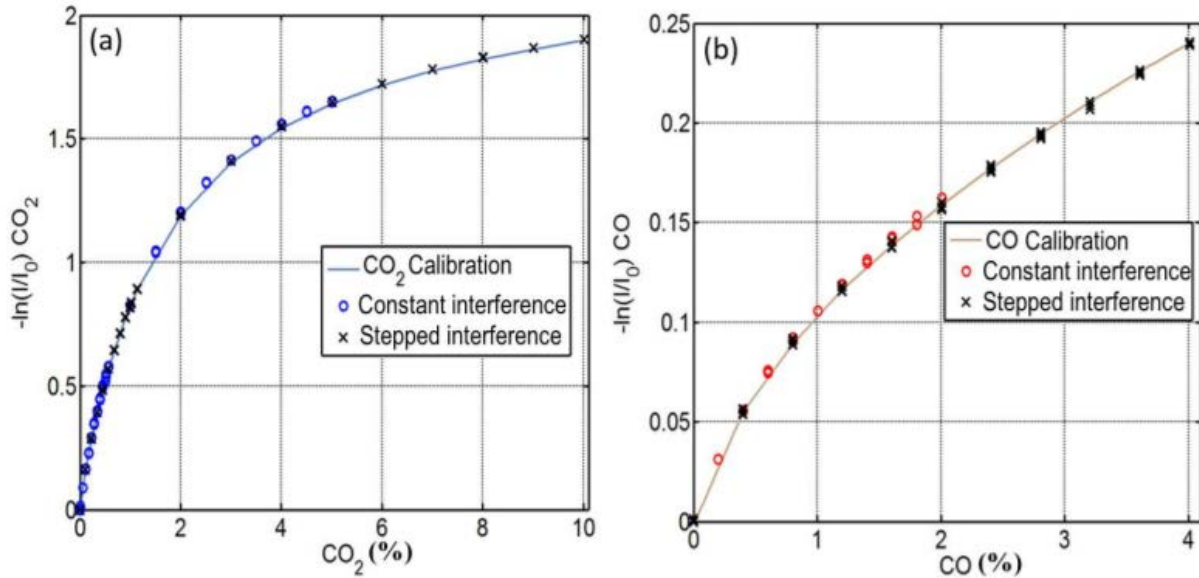


Figure 21: Results from the cross-interference measurements

The performance of the sensor as it is has been discussed so far was published by Kyle Thurmond and co-authors in a paper of the journal Applied Spectroscopy [14]. However, since this publication, the performance of the LEDs has been increased by re-evaluating the driving electronics as was discussed in chapter 3. For the reevaluation, Alicat mass flow controllers (MC series 10SCCM and 50SCCM) which contained, some noise concentrations at low concentrations, were used. With these enhancements, the CO₂ detectivity limit was improved to 8ppm and the CO detectivity limit was improved to 300ppm, a 73.3% and 25% reduction respectively.

4.3 Time Resolutions

The analysis procedure provides for 1kHz (1-ms) measurement rate. For each measurement, the detector signal was recorded at 106 Hz for one second to obtain 106 samples. The data was split in to 1000 time bins each containing 1000 data points, and a Fast Fourier Transform (FFT) was performed on each bin in order to determine the signals (irradiance surrogate) from the three LEDs. After normalizing the two measurement LED signals using the reference LED signal, the absorbance values were calculated per Eq.1, but including a factor to account for differing optical losses between the various LED sources; i.e., the absorbance was calculated as $-\ln(4.2 I_{3.6} c_{CO_2})$ for CO₂ and $-\ln(14.7 I_{3.6} c_{CO})$ for CO, where c_{CO_2} and c_{CO} are the loss factors determined from measurement of a non-absorbing N₂ sample. This analysis procedure provided for simultaneous CO₂ and CO measurements at 103 Hz. For the steady state measurements, the standard deviation between the 1000 bins was used to quantify measurement uncertainty. Because the analysis procedure provides for 103 Hz measurement rate, the sensor is theoretically able to record fluctuations in absorbance of up to 500Hz (the Nyquist

frequency) without aliasing, and practically able to accurately resolve transients of up to 250Hz. This temporal resolution is sufficient for engine-development and -research applications. The temporal resolution could be further improved by improving the LED throughput (and signal-to-noise ratio) as discussed above and faster signal acquisition, thus enabling use of shorter analysis bins. The intrinsic sensor speed, independent of gas dynamics associated with the measurement cell, was characterized via temporal-resolution measurements, and demonstrated the fastest transients the sensor can resolve. Although gas dynamics will certainly limit temporal resolution of the sensor configuration using the measurements cell, the intrinsic sensor speed is relevant to direct sensor applications; e.g., where the measurement cell is replaced by an engine intake runner for line-of-sight measurements. Moreover, the intrinsic temporal resolution establishes a baseline performance standard that can be references to assess sensor improvements. For these experiments, the combined-LEDs beam was modulated from 25 to 400Hz using a 10- window optical chopper with various layers of polymer (polypropylene office material, Scotch tape, etc.) placed over three of the ten windows as shown in Figure 22. As the chopper rotates, it effectively turns the LED beam on and off via the open and solid portions of the wheel, respectively, and the polymer-covered windows simulate absorption; it is known that the polymer has broad absorption features around the 3.6 μm Reference LED emission region. Of course, the intrinsic sensor response is independent of the specific LED used for the assessment, and so the same response would be measured if real or synthetic absorption occurred at the CO₂ or CO wavelengths.

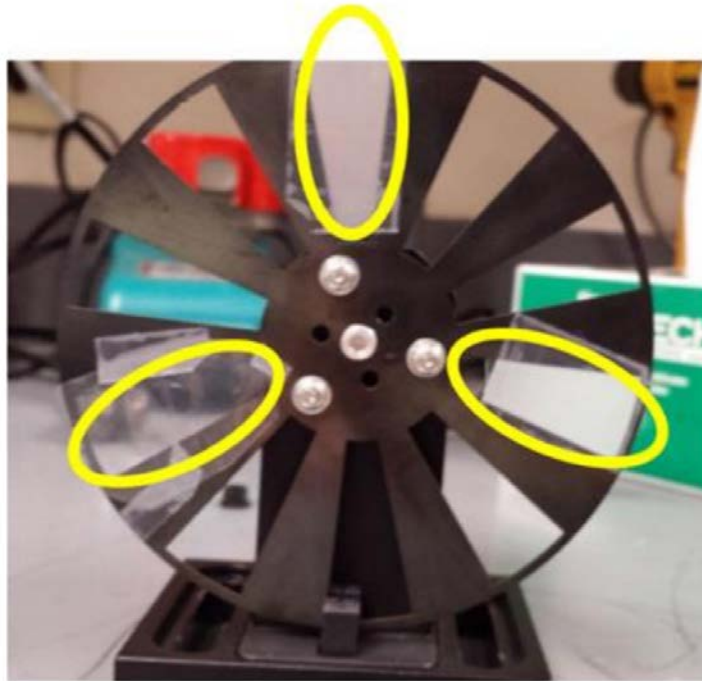


Figure 22: Optical chopper used for beam modulation in the temporal response studies

Figure 23 shows results of the temporal response measurements to indicate resolution sufficient for intra-cycle-resolved engine measurements. The high-signal peaks are associated with the seven open chopper-wheel windows in Figure 22, the zero-signal points are associated with the ten solid windows, and the intermittent-signal peaks with the three polymer-covered windows

which synthesized absorption. The magnitude of the intermediate peaks reflects the number of polymer layers covering each chopper window, with lower signal level indicating greater number of absorbing layers. The clear 2-3-2 temporal pattern of the high-signal peaks reflects the spatial geometry of Figure 22, and can be used to assign the intermediate peaks to specific windows. Specifically, the intermediate peaks surrounding the three high-signal peaks are the two lower circled windows in Figure 22 surrounding the three open chopper windows. Moreover, these two intermediate peaks have the greatest (ca. 1a.u.) and least (ca. 0.35a.u.) intermediate signal level, indicating the least and greatest number of absorbing polymer layers, respectively. Correspondingly, the middle (ca. 0.6a.u.) intermediate signal corresponded to the chopper window opposite the three open windows, and had the intermediate number of absorbing polymer layers. This logical interpretation of the Figure 23 patterns was consistent with the actual configuration of the chopper (i.e., number and distribution of absorbing layers), and is evidence of the sensor's temporal resolution beyond the ability to resolve individual chopper-window events. At 250Hz modulation, a chopper window should pass the LED beam every 4ms, which is consistent with the results shown in Figure 23a. This corresponds to 23 crank-angle-degrees (CAD) for an engine operating at 1000RPM, and indicates the ability to resolve transients on the order of individual (intake or exhaust) valve events. While the experiments performed do not account for sources of interference that may be present in actual engine measurements, the results illustrate that the sensor has sufficient temporal resolution for resolving cylinder-to-cylinder and cycle-to-cycle variations in intake charge and combustion completion; combustion uniformity can be accessed via intake manifold measurements, and combustion-completion fluctuations could be assessed via CO-CO₂ ratio variations [13].

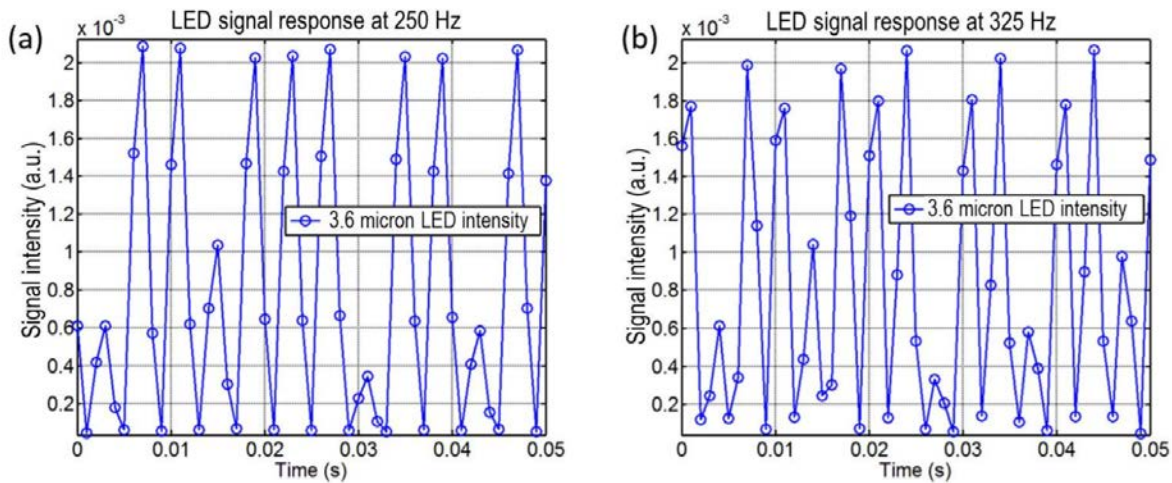


Figure 23: Temporal-resolution measurement results at (a) 250Hz, (b) 325Hz

Faster transients could be resolved with alternate analysis bin size or higher DAQ speed. The 250Hz modulation results in Figure 23a indicate measurements below the Nyquist limit and synchronous with the measurement rate; in this synchronous case, there are exactly 4 measurements per modulation cycle resulting in consistent signals for the various open-window peaks. Figure 23b demonstrates the nature of transitioning beyond faithful transient

characterization. Although 325Hz modulation is below the Nyquist limit and the results clearly show the patterns of the open and synthetic-absorption windows, the transients show more temporal variations compared to the 250Hz results. This is due to the nonsynchronous analysis and modulation; specifically, at 325Hz, there are ca. 3.08 measurements per modulation cycle, causing the measurements to progressively walk through the modulations. This is manifested by the varying peak heights through the chopper revolution. For instance, the open-window high signal-level peaks vary in magnitude because different points around the modulation peaks are sampled in this nonsynchronous mode. Similarly, there are differences in transient shape for identical transients in subsequent chopper modulations; e.g., the high-peak pair around 0.009s and 0.042s in Figure 24b corresponds to the same chopper window, as does the intermediate peak at ca. 0.013s and 0.048s. This demonstrates the onset transient-response error, and such transient distortion would continue with increasing modulation rate until it was completely unresolved at the Nyquist limit. While the sensor has been demonstrated as having sufficient temporal resolution for engine-research applications, the temporal resolution could be further extended by increasing the measurement rate. This could be implemented by increasing the DAQ rate or modifying the analysis procedure to use smaller temporal analysis bins; e.g., the temporal resolution could be doubled to 2kHz by using 500 rather than 1000 data points per FFT analysis bin. Although the signal, noise and other practical tradeoffs would have to be considered, this provides a general framework for further extending the sensor temporal resolution.

4.4 Environmental Chamber Evaluations

An environmental chamber, which is shown in Figure 24 below, was used for evaluation of the sensor at near-space conditions. The chamber was constructed by Dr. Peale et al and consists of a large steel bell jar that is 0.5m in diameter and 0.8m in height [21]. Inside the bell jar is a copper shroud wrapped in copper tubing which allows the flow of liquid nitrogen (LN2) which cools the interior the chamber. Feedthrough lines at the base of the chamber allowed electrical connections for controlling and monitoring the sensor as well as for feeding gas flow, such as controlled CO and CO2. A high volume roughing pump was used to pump the chamber down to a pressure and temperature of approximately 2Torr and -15°C, respectively. The first round of testing in the chamber was solely with the sensor to confirm everything operated as expected. This was also the first time the TECs were to be used in reverse. The test ran for an hour with success. The LEDs and detector thermal management plan were very successful. However, another test was run without cooling the chamber (ambient temperature, low pressure), and it was discovered that the driver modules had trouble maintaining their temperature.



Figure 24: Dr. Peale's environmental chamber at UCF

4.5 HASP Integration Thermal/Vacuum Testing

The second round of environmental chamber testing completed at NASA's Columbia Scientific Balloon Facility's Thermal Vacuum Chamber located in Palestine Texas, as is shown in Figure 25 below. The test duration was 8 hours and 30 minutes. The temperature range was -60°C to 50°C and the pressure range was 8mbar to 1bar. Throughout the test, the system performed as expected except for a small issue involving downlinking random noise. It was discovered that this was due to the fact that one regulator was non-isolated; replacing it with an isolated regulator resolved this problem.

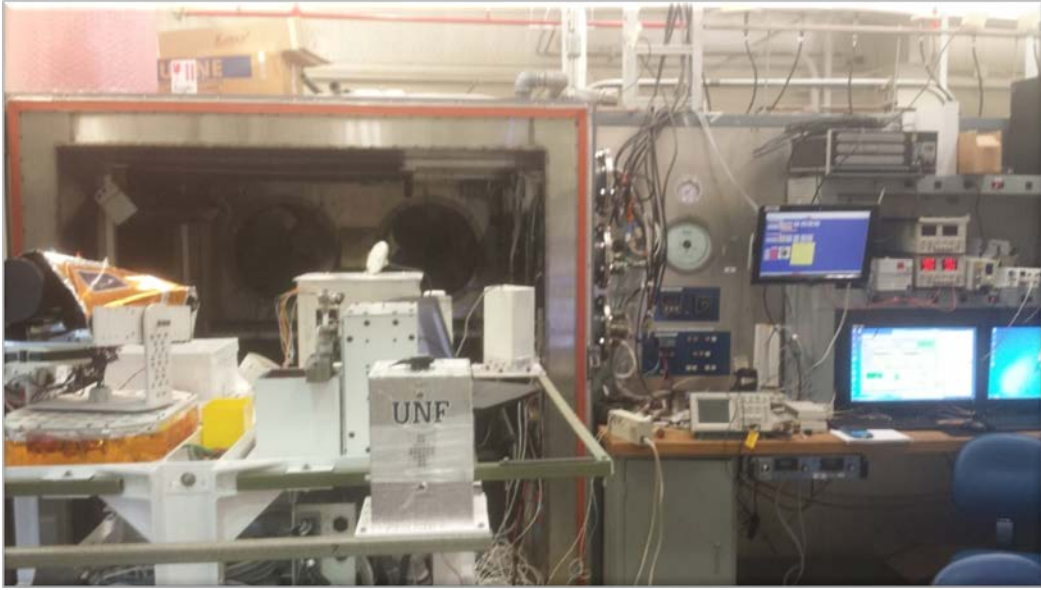


Figure 25: Environmental testing chamber at CSBF

CHAPTER 5: HASP Flight

5.1 Telemetry

I. Downlink Telemetry Specifications:

- A. Serial data downlink format: Stream Packetized (circle one)
- B. Approximate serial downlink rate (in bits per second)
NA
- C. Specify your serial data record including record length and information contained in each record byte.
NA
- D. Number of analog channels being used:
1
- E. If analog channels are being used, what are they being used for?
A steady 5V output on the NI DAQ will be generated in the running VI and will be used to determine healthy system operation. If all systems are operational the VI will generate a 5V signal to be read by Analog Channel 1 (Pin K and L). In event of system or component failure, the VI will cease its 5V output resulting in a zero reading. If 5V signal ceases a power off/on command will be given to restart/reboot system.
- F. Number of discrete lines being used:
NA
- G. If discrete lines are being used what are they being used for?
NA
- H. Are there any on-board transmitters? If so, list the frequencies being used and the transmitted power.
No
- I. Other relevant downlink telemetry information.
It is requested that HASP GPS Time and Position Data be streamed to the payload via the serial connection in a continual interval of 30 seconds. This data will be read by the NI cRIO-9031 DAQ via an adapter to a RJ-50 10-position modular jack and saved with primary collected data during flight operation.

II. Uplink Commanding Specifications:

- A. Command uplink capability required: Yes No (circle one)
- B. If so, will commands be uplinked in regular intervals: Yes No (circle one)

C. How many commands do you expect to uplink during the flight (can be an absolute number or a rate, i.e. *n commands per hour*)

NA

D. Provide a table of all of the commands that you will be uplinking to your payload

NA

E. Are there any on-board receivers? If so, list the frequencies being used.

NA

F. Other relevant uplink commanding information.

NA

III. Integration and Logistics

A. Date and Time of your arrival for integration:

Date of Arrival: August 1st, 2016 Time: 10 AM

Date of Departure: August 5th, 2016 Time: 7 PM

B. Approximate amount of time required for integration:

Estimation of 1 hour (Integration time is expected to be much less than 1 hour as system will already be attached to payload plate and will only require plate attachment to HASP system and connection of the RS-232 Serial Connector and EDAC 516 Connector)

C. Name of the integration team leader:

Michael Villar

D. Email address of the integration team leader:

mvillar@knights.ucf.edu

E. List ALL integration participants (first and last names) who will be present for integration with their email addresses:

Michael Villar (mvillar@knights.ucf.edu)

Justin Urso (justin.urso13@knights.ucf.edu)

Akshita Parupalli (akshita.parupalli@Knights.ucf.edu)

F. Define a successful integration of your payload:

Successful integration of the Hazardous Gases for Harsh Environments LED Sensor with the HASP platform includes: successful mechanical attachment of Payload 09 to the HASP system and connection of HASPs Power system; confirming the functionality of individual LED operation, TEC control and Thermocouple readings; proper signal collection via the detector and data storage in the National Instruments cRIO DAQ; secondary confirmation of same functionality while undergoing thermal-vacuum testing and successful completion of thermal vacuum test.

Mechanical system:

- Successful mechanical fit to the platform

Electrical system:

- Successful power up
- Current draw lies within expectations

Communication system:

- Successful communication with HASP Platform
- Verification of Data Collection and Storage

Environmental System Check:

- Successful thermal vacuum test

G. List all expected integration steps:

- Mechanically mount the payload to the platform
- Connect power cable
- Verify Current and Voltage draw to:
 - NI cRIO DAQ
 - LEDs 1-3
 - Detector
 - Driving Electronics
- Connect communication cable
- Verify that the communication with the platform is working
- Verify proper Data Collection and Storage
- Successfully complete Thermal Vacuum Test

H. List all checks that will determine a successful integration:

All Steps are covered in parts F/G

I. List any additional LSU personnel support needed for a successful integration other than directly related to the HASP integration (i.e. lifting, moving equipment, hotel information/arrangements, any special delivery needs...):

NA currently.

J. List any LSU supplied equipment that may be needed for a successful integration:

Wrenches, Pliers, Wire Cutters/Strippers, Hex Keys

5.2 Flight-line Setup and Pre-Launch Checkout Procedures

T= -2.0

- Power up system
 - Remotely check voltage from pin K and L on EDAC 516.
 - If 5V, power up successful.
 - Otherwise, power cycle.
 - This item is to be completed by HASP personnel.

As system is designed to be autonomous, no other controls needed.

A. Flight-line Setup Period

- Fill gas cell
- Student will have cylinder of test gas (mix of CO, CO₂, and N₂) and will fill cell.

B. Pre-launch Checkout Period:

N/A

II. Flight Operation Procedures

- System is autonomous, no inputs needed.
 - GPS data will be recorded to correlate data to time and position.
- Power Cycle
 - If 5V Analog signal on pin K and L ceases, transmit power off/power on commands.
 - Command Successful if 5V signal re-appears on analog line.
 - Critical Command
 - 5V signal indicates functional system power to payload 09

A. Uplink Command List: N/A

B. Commands to be executed during climb-out: N/A

C. Flight Configuration Setup: N/A

D. Failure Response: N/A

E. Termination: N/A

III. Recovery, Packing and Shipping Instructions

A. Recovery Instructions:

- a. Gas cell will contain CO, CO₂, and N₂ mixture, concentrations low enough that if needed can be vented into atmosphere by opening valve.
- b. Gas cell will be at atmospheric pressure.
- c. **Sensitive optical equipment in system**

B. Packing Instructions:

- a. Package and ship attached to HASP board in an upright position.

C. Shipping:

- a. Shipping Materials will be provided with pre-paid labels to return to UCF

5.3 Flight Results

UCF's payload was successfully returned Sep. 14th and a breakdown of the system was completed to access the onboard flight data. This includes writing a Matlab script to parse all of the 697 collected measurements and correlate the peak intensities of the captured LED signals with the environmental data (Pressure/Temp) throughout the entire flight. The sensor modulates its three LEDs at different wavelengths so that a FFT can be done to the stored signal to determine the peak intensity of each LED. The Matlab script used to parse and analyze all of the flight data is attached in the appendix at the end.

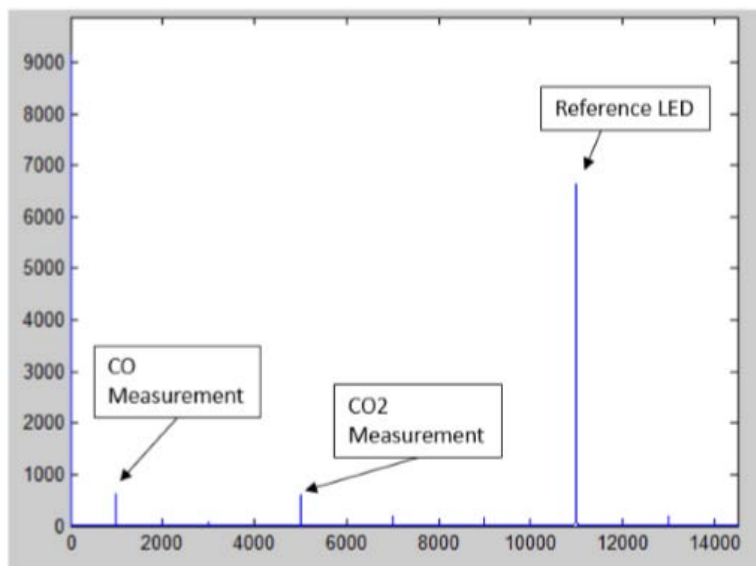


Figure 26: LED Magnitudes

Temperature and Pressure effects the intensity of this signal and when the Temp and Pressure data from the flight is added into the data it will output the concentration measurements of CO and CO2 in our gas cell (Which should read a constant measurement).

Flight Conditions:

- **Max Altitude:** 123,546 ft.
- **Temperature Range:** -54.47 °F to 53.76 °F
- **Pressure Range:** 0mbar to 910mbar
- **Float Duration:** 15h:08m:54s
(Total: 18h:09m:30s)

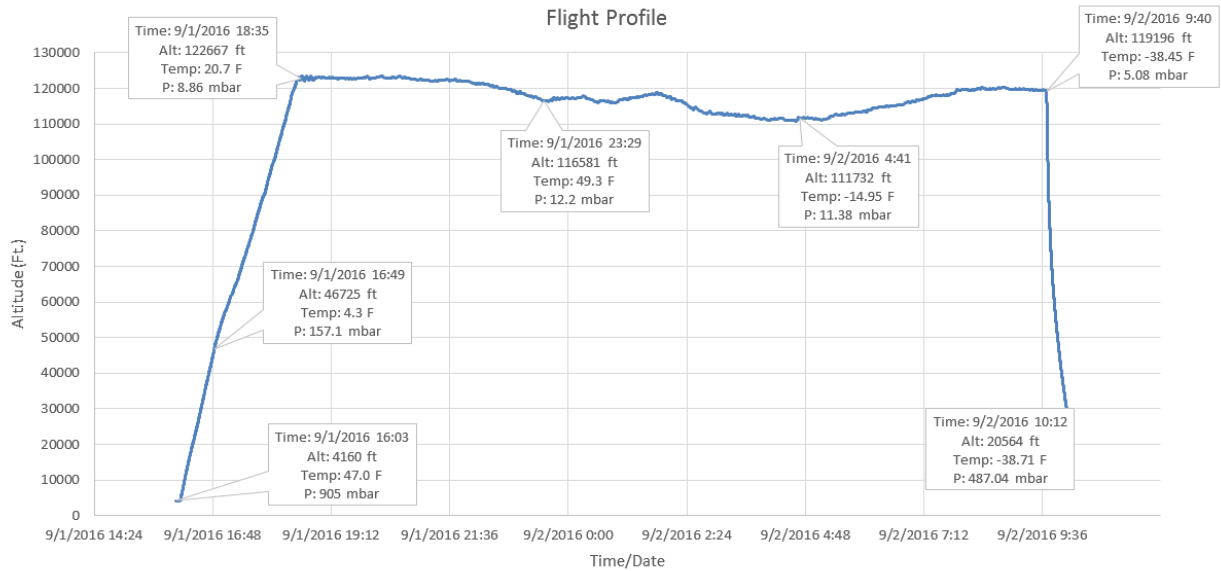


Figure 27: Flight Profile

The TECs under standard operation should keep the LEDs at a constant set temperature of 0°C. The actual temperature profile is shown below. Each LED’s output varies with temperature so a calibration equation has been established to eliminate the temperature variance in the measurements.

The system was placed back into the environmental chamber to test to make sure that the systems LED’s post flight measurements were consistent with pre-flight measurements (LED outputs pre-flight and post-flight were found to be equal). This was established to provide confident that the tests for the temperature variance calibration equation would be applicable to the flight data. Equal pre- and post- flight LED output measurements proved that the system did not alter during flight.

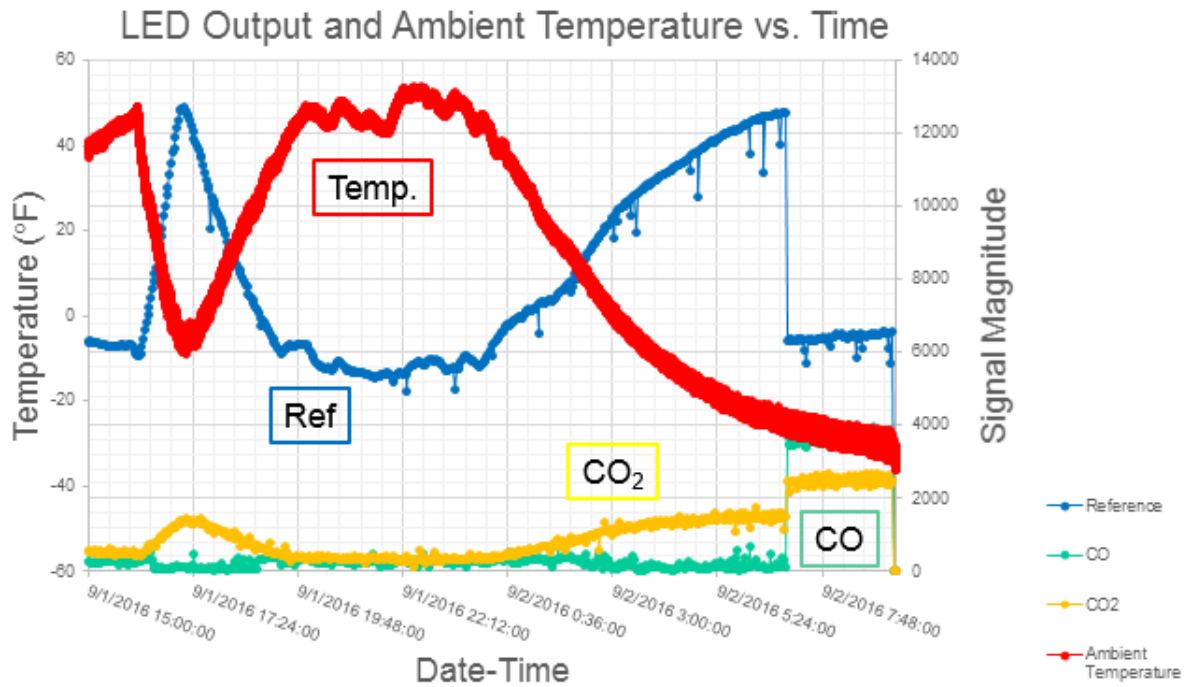


Figure 28: LED Output and Ambient Temperature vs. Time

5.5 Post-Flight

A breakdown of the system was undertaken to understand what components broke or failed during flight. The test began with structural integrity, which revealed minor structural damage due to the landing impact. The main points of damage were an optical post that had sheared off near the LED end of the optics, as is shown in Figure 29 below, and a few screws that had come loose as can be seen in Figure 30. It is unclear if the vibrations that caused the screws to loosen were from transporting the system from the landing site or if they occurred flight. Analysis of the driver circuits showed that the connection pins had come undone in the impact and had bent during transport, but after straightening out the connections and testing the integrity of the drivers, they were shown to be fully functional. All of the internal electronics were tested and still function properly. All regulators still work correctly and show no signs of damage. Lastly, the LEDs and the detector were tested by independently attaching the LEDs to a function generator and a secondary detector to test functionality. All LEDs and the detector and still functioning properly.



Figure 29: Post-flight pictures showing the sheared-off optical screws



Figure 30: Top view of the system showing missing screws

CHAPTER 6: Conclusions and Future Work

6.1 Conclusion

A sensor for simultaneous detection of CO and CO₂ was developed using low-cost LEDs. The sensor was able to detect concentration changes as small as 8ppm and 300ppm for CO₂ and CO, respectively, with no cross-interference between CO₂ and CO. The sensor was subjected to a harsh near space environment of -55 to 60°F at ~1 to 900mbar and altitude of 120,000+ ft for a duration of 18h30min. This sensor design achieved on-board monitoring, diagnostics and control of performance fluctuations associated with these CO and CO₂, including EGR. The method and design developed here is applicable to developing sensors for a variety of gases, as a number of important gases, such as NO₂, N₂O, and CH₄, have fundamental absorption bands in the MIR spectral region. Several insights were gained regarding increasing the sensors detection limit, sensitivity and temporal resolution. The CO₂ sensitivity was up to 10-times greater than CO because a greater number of CO₂ absorption features were measured by the broadband measurement. However, the CO₂ sensitivity degraded much faster than CO (although CO₂ sensitivity remained greater throughout) at higher concentrations because the stronger CO₂ absorption transitions entered saturation before the weaker CO transitions. The CO sensitivity and detection limit could be improved without compromising the cross-interference performance by using a broader LED bandpass filter that incorporated the longer-wavelength CO₂ absorption transitions (in the ca. 4.7- 5um region) clipped by the current filter. Temporal resolution could be further improved by using higher DAQ speeds and/or reducing the FFT analysis bin size; this could be further enabled by increasing the sensor SNR by increasing LED emission throughput via improved optical design. Nevertheless, the LED sensor has demonstrated performance for advancing engine and combustion research in its existing state, and these insights provide a pathway for further expanding the range of applicability. The current detectivity limit for CO and CO₂ still has a lot of room for improvement from the ~80% optical signal loss and to reduction electrical noise. The use of beam splitters has significant consequences to signal loss, other forms of beam multiplexing should be considered such as tightly spaced arrays. Reducing optical losses due to the LED's incoherent nature was tricky, most of these losses are at the detector face which is 1x1mm. A larger detector face generally reduces detectivity and makes it more sensitive to noise. Currently the circuits experience some faint cross-over noise from the other LEDs signals. Finally, for test at UCF we used Alicat mass flow controllers which experience have a lot of low end noise. These issues carry over into the sensors sensitivity. In addition to the lab-based sensitivity, detection limit, noise and cross interference addressed here, engine applications require additional considerations including, background IR interference, interference from other combustion products such as nitrous oxide (N₂O), and vibration-induced noise. The frequency based analysis procedure would aid in rejecting some interference and noise sources possible in actual engine experiments, as signals at frequencies other than those specified for the LED modulation are be rejected. Another approach that has been used to address background interference is to directly measure that background by momentarily turning off the LEDs and implementing an offset correction. N₂O has absorption features of comparable magnitude to and overlapping those of CO and CO₂, and is thus a source of potential interference. Vibrations should not impact the

performance of a well-designed and mechanically stable diagnostic based on extractive sampling, such as that of the current sensor. In separate work using a similar sensor designed to measure CO₂, it has been observed that the vibration of hollow-waveguides used for probe-based on-engine measurements increased the uncertainty in measurements from 0.1% in vibration-free laboratory calibrations to 1.1%; however, these uncertainties were much less than the actual CO₂ concentration fluctuations and did not limit practical application of the diagnostic [13]. It is expected that vibrations would impact a probe-based configuration of the current sensor's performance similarly.

6.2 Future Work

Current development of the sensor is in adaptations for space vehicles and any environments that may be encountered during space flight. Additional flights are planned to follow and may also include parabolic flights or missions to the International Space Station (ISS). The goal is to develop the hardware so that it is a rugged and a viable technology for a variety of sensor applications in a variety of environments. It is therefore crucial that the hardware can reject heat at low pressures, survive low temperature operation, have low drift (stable output), remain low power, and be insensitive to humidity. As the hardware is further refined it should become more compact with more efficient multiplexing approaches. This may take the form of tightly spaced arrays of LEDs which use custom integrated lenses. The driving electronics will also need to be refined to a more efficient design as the current system produces excessive waste heat.

- Miniaturization: Sensor design and housing design must be optimized for spacecraft environment. This would require a caged design that will house every component keeping the weight to the allowable values
- Broader Species Detection: N₂O (oxidizer), HCN (cabin hazard), H₂O, etc.
 - Improve detection limits through:
 - Optimizing optical arrangements
 - Developing stable LED driver circuits
 - New filter selections
 - Adding additional LEDs
- Develop models for broad spectrum absorption which will allow on the fly path length adjustments and theoretical designing for other gas targets
 - Demonstrate technique for other wavelengths to target more species (e.g. N₂O)

CHAPTER 7: Presentations and Publications

7.1 NSMMS/CRASTE Presentation

“Progress in Development and Testing of a LED-Based Fire and Hazard Detection Sensor for Space Vehicles,” 2016 National Space & Missile Materials Symposium (NSMMS) & the Commercial and Government Responsive Access to Space Technology Exchange (CRASTE) Westminster, Colorado.

CRASTE’s focus is on matching system integrators with subsystem technology providers to enable new responsive space access capabilities. Special focus is given to the integration of emerging technologies and emerging space access architectures to satisfy new and existing markets.

7.2 COE CST ATM6 Presentation

“Task 311-UCF, Robust and Low-Cost LED Absorption Sensor” Center of Excellence Commercial Space Transportation 6th Annual Technical Meeting Las Cruces, New Mexico.

Congress authorized Air Transportation Centers of Excellence under the Federal Aviation Administration Research, Engineering and Development Authorization Act of 1990. This legislation enables the FAA to work with universities and their industry partners to conduct research in environment and aviation safety, and other activities to assure a safe and efficient air transportation system. With the establishment of the COE CST in offices of FAA AST, research will extend to cutting-edge technologies and infrastructure for private human spaceflight and orbital debris mitigation.

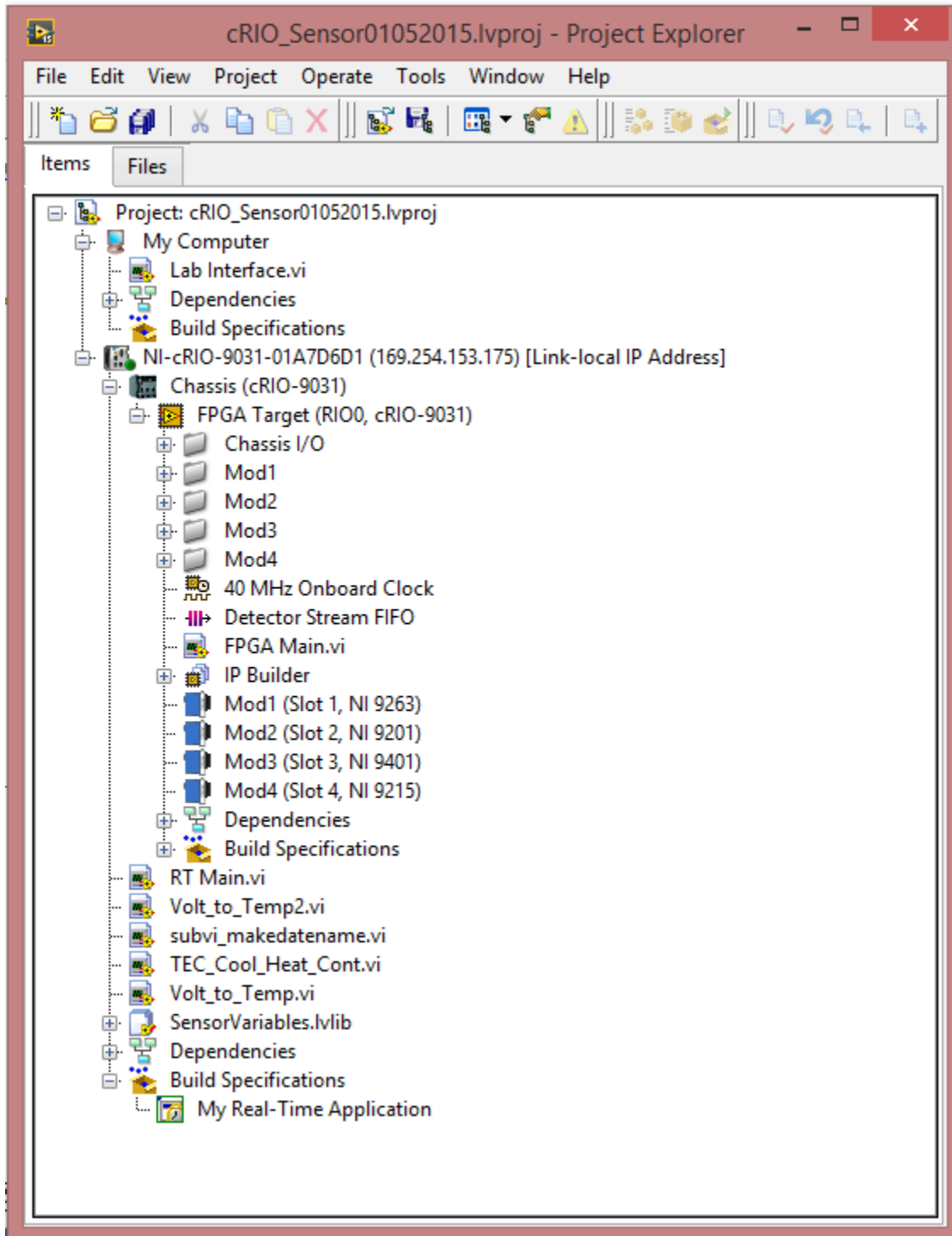
REFERENCES

- [1] 2013, "International Energy Outlook 2013," D. o. Energy, ed. [http://www.eia.gov/forecasts/ieo/pdf/0484\(2013\).pdf](http://www.eia.gov/forecasts/ieo/pdf/0484(2013).pdf).
- [2] Manley, D. K., McIlroy, A., and Taatjes, C. A., 2008, "Research needs for future internal combustion engines," *Physics Today*, 61, pp. 47-52.
- [3] Alexander, L., Allen, S., Bindoff, N., Breon, F.-M., Church, J., Cubasch, U., Emori, S., Forster, P., Friedlingstein, P., Gillett, N., Gregory, J., Hartmann, D., Jansen, E., Kirtman, B., Knutti, R., Kanikicharla, K. K., Lemke, P., Marotzke, J., Masson-Delmotte, V., Meehl, G., Mokhov, I., Piao, S., Ramaswamy, V., Randall, D., Rhein, M., Rojas, M., Sabine, C., Shindell, D., Talley, L., Vaughan, D., and Xie, S.-P., 2013, "The IPCC Fifth Assessment Report Climate Change 2013," Intergovernmental Panel on Climate Change, http://www.climatechange2013.org/images/uploads/WGIAR5_WGI12Doc2b_FinalDraft_All.pdf.
- [4] Zheng, M., Reader, G. T., and Hawley, J. G., 2004, "Diesel engine exhaust gas recirculation— a review on advanced and novel concepts," *Energy Conversion and Management*, 45(6), pp. 883-900.
- [5] Chandler, F., Ambrose, R., Biegel, B., Brown, T., Carter, J., Culbert, C., Edwards, C., Fox, J., Glaessgen, E., Hurlbert, K., Israel, D., Johnson, L., Kliss, M., Linne, D., Meador, M., Mercer, C., Meyer, M., Motil, B., Munk, M., Nesnas, I., Prince, J., Ryan, R., Scott, J., and Siochi, E., 2015, "2015 NASA Technology Roadmaps," NASA, [ed.http://www.nasa.gov/offices/oct/home/roadmaps/index.html](http://www.nasa.gov/offices/oct/home/roadmaps/index.html).
- [6] Ren, W., Farooq, A., Davidson, D. F., and Hanson, R. K., 2012, "CO concentration and temperature sensor for combustion gases using quantum-cascade laser absorption near 4.7 μm ," *Applied Physics B*, 107(3), pp. 849-860.
- [7] Farooq, A., Jeffries, J., and Hanson, R. K., 2008, "CO₂ concentration and temperature sensor for combustion gases using diode-laser absorption near 2.7 μm ," *Applied Physics B*, 90(34), pp. 619-628.
- [8] Teichert, H., Fernholz, T., and Ebert, V., 2003, "Simultaneous In Situ Measurement of CO, H₂O, and Gas Temperatures in a Full-Sized Coal-Fired Power Plant by Near-Infrared Diode Lasers," *Applied Optics*, 42(12), pp. 2043-2051.
- [9] Mihalcea, R. M., Baer, D. S., and Hanson, R. K., 1998, "Advanced diode laser absorption sensor for in situ combustion measurements of CO₂, H₂O, and gas temperature," *Sumposium (International) on Combustion*, 27(1), pp. 95–101.
- [10] Schultz, I. A., Goldenstein, C. S., Jeffries, J. B., and Hanson, R. K., 2012, "TDL Absorption Sensor for In Situ Determination of Combustion Progress in Scramjet Ground Testing," *Aerodynamic Measurement Technology, Ground Testing, and Flight Testing Conference*, 28.

- [11] Silver, J. A., 1992, "Frequency-modulation spectroscopy for trace species detection: theory and comparison among experimental methods," *Applied Optics*, 31(6), pp. 707-717.
- [12] Rothman, L. S., Gordon, I. E., Babikov, Y., Barbe, A., Benner, D. C., Bernath, P. F., Birk, M., Bizzocchi, L., Boudon, V., Brown, L. R., Campargue, A., Chance, K., Cohen, E. A., Coudert, L. H., Devi, V. M., Drouin, B. J., Fayt, A., Flaud, J. M., Gamache, R. R., Harrison, J. J., Hartmann, J. M., Hill, C., Hodges, J. T., Jacquemart, D., Jolly, A., Lamouroux, J., Roy, R. J. L., Li, G., Long, D. A., Lyulin, O. M., Mackie, C. J., Massie, S. T., Mikhailenko, S., Müller, H. S. P., Naumenko, O. V., Nikitin, A. V., Orphal, J., Perevalov, V., Perrin, A., Polovtseva, E. R., Richard, C., Smith, M. A. H., Starikova, E., Sung, K., Tashkun, S., Tennyson, J., Toon, G. C., Tyuterev, V. G., Wagner, G., Müller, H., and Smith, M., 2013, "The HITRAN2012 molecular spectroscopic database," *Journal of Quantitative Spectroscopy and Radiative Transfer*.
- [13] Yoo, J., Prikhodko, V., Parks, J. E., Perfetto, A., Geckler, S., and Partridge, W. P., 2015, "Fast Spatially-Resolved EGR Distribution Measurements in an Internal Combustion Engine using Absorption Spectroscopy," *Applied Spectroscopy* #(#), pp. #-#.
- [14] Thurmond, K., Loparo, Z., Partridge, W. P., and Vasu, S., 2016, "A Light-Emitting Diode (LED) Based Absorption Sensor for Simultaneous Detection of Carbon Monoxide and Carbon Dioxide," *Applied Spectroscopy*.
- [15] Puton, J., Jasek, K., Siodłowski, B., Knap, A., and Wiśniewski, K., 2002, "Optimisation of a pulsed IR source for NDIR gas analysers," *Opto-Electronics Review*, 10(2), pp. 97-103.
- [16] Laine, D., Al-Jourani, M., Carpenter, S., and Sedgbeer, M., "Pulsed wideband IR thermal source," *Proc. Optoelectronics, IEE Proceedings-, IET*, pp. 315-322.
- [17] Matveev, B. A., Gavrilov, G. A., Evstropov, V. V., Zotova, N. V., Karandashov, S. A., Sotnikova, G. Y., Stus, N. M., Talalakin, G. N., and Malinen, J., 1997, "Mid-infrared (3-5 μm) LEDs as sources for gas and liquid sensors," *Sensors and Actuators B: Chemical*, 39(1-3), pp. 339-343.
- [18] Ioffe, I., 2013, "LEDs for the mid-infrared region of the spectrum (2-6 micrometers)," Ioffe Institute, http://www.ioffeled.com/index.php?option=com_content&view=article&id=52&Itemid=103.
- [19] Perry, F., 2013, "IR Detectors from Vigo Systems," Bosten Electronics, <http://www.boselec.com/products/documents/-VigoCatalog11-5-13WWW.pdf>.
- [20] 2013, "Zemax," Radiant Zemax, <http://www.radiantzemax.com/en>.

- [21] Maukonen, D., Fredricksen, C. J., Muraviev, A. V., Alhasan, A., Calhoun, S., Zummo, G., Peale, R. E., and Colwell, J. E., "Planetary Atmospheres Minor Species Sensor (PAMSS)," Proc. SPIE Sensing Technology+ Applications, International Society for Optics and Photonics, pp. 91130N-91130N-91138.

APPENDIX: DAQ CODE (VI's)



FPGA Main

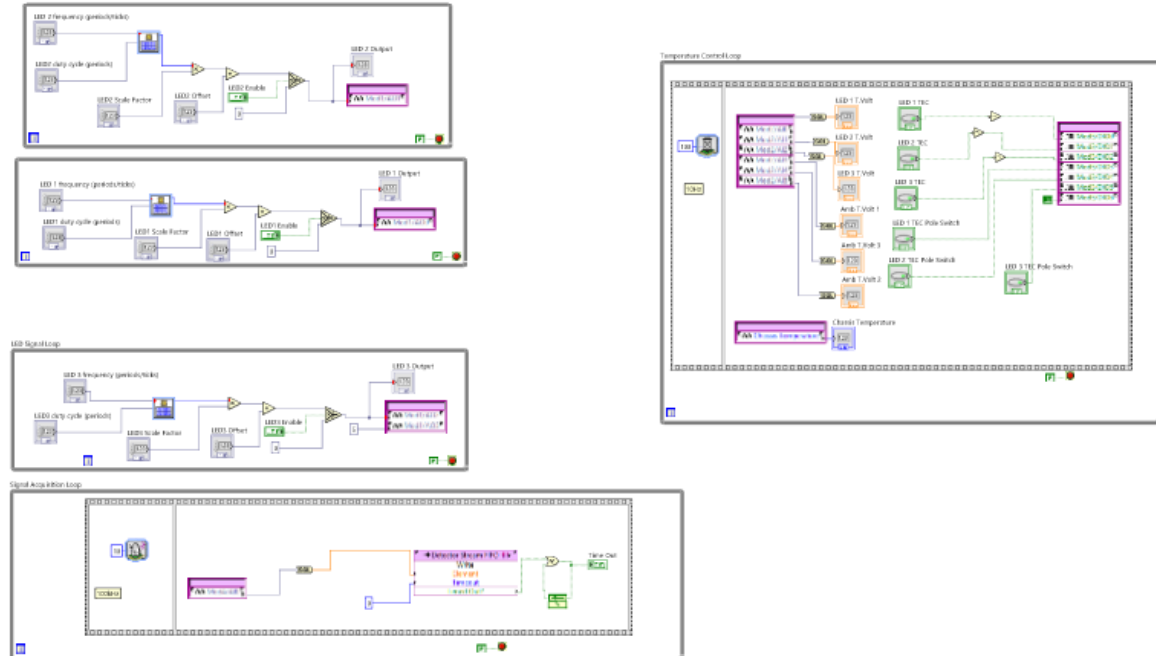


FPGA Main.vi

C:\Users\Mike\Desktop\cRIO - Copy\FPGA Main.vi

Last modified on 7/27/2016 at 7:26 PM

Printed on 12/9/2016 at 2:06 PM



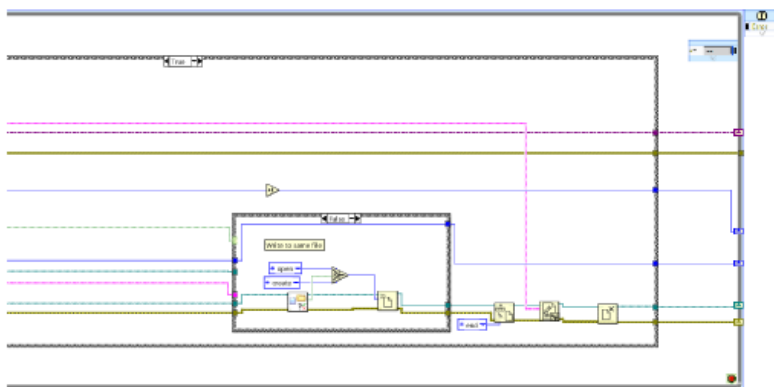
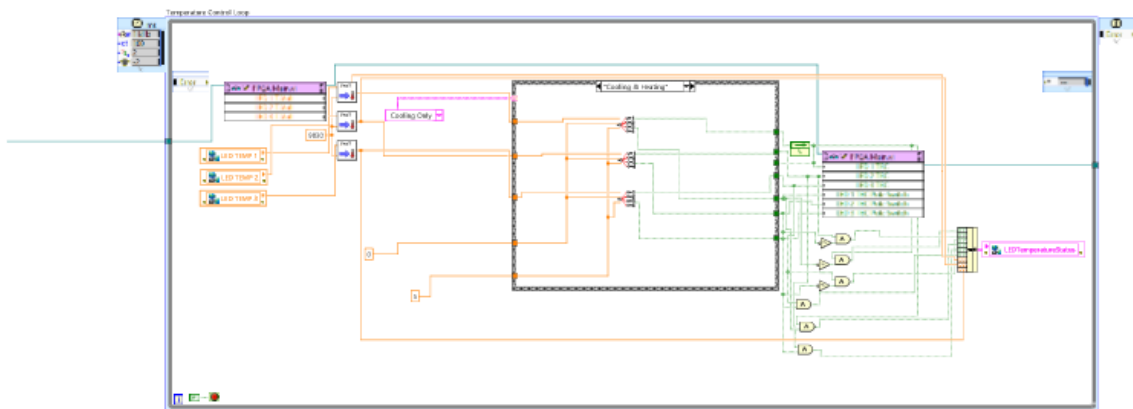
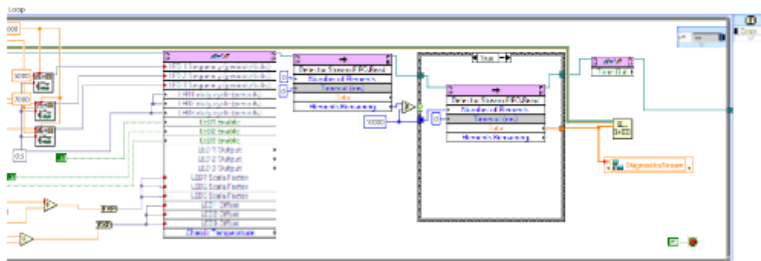


RT Main.vi

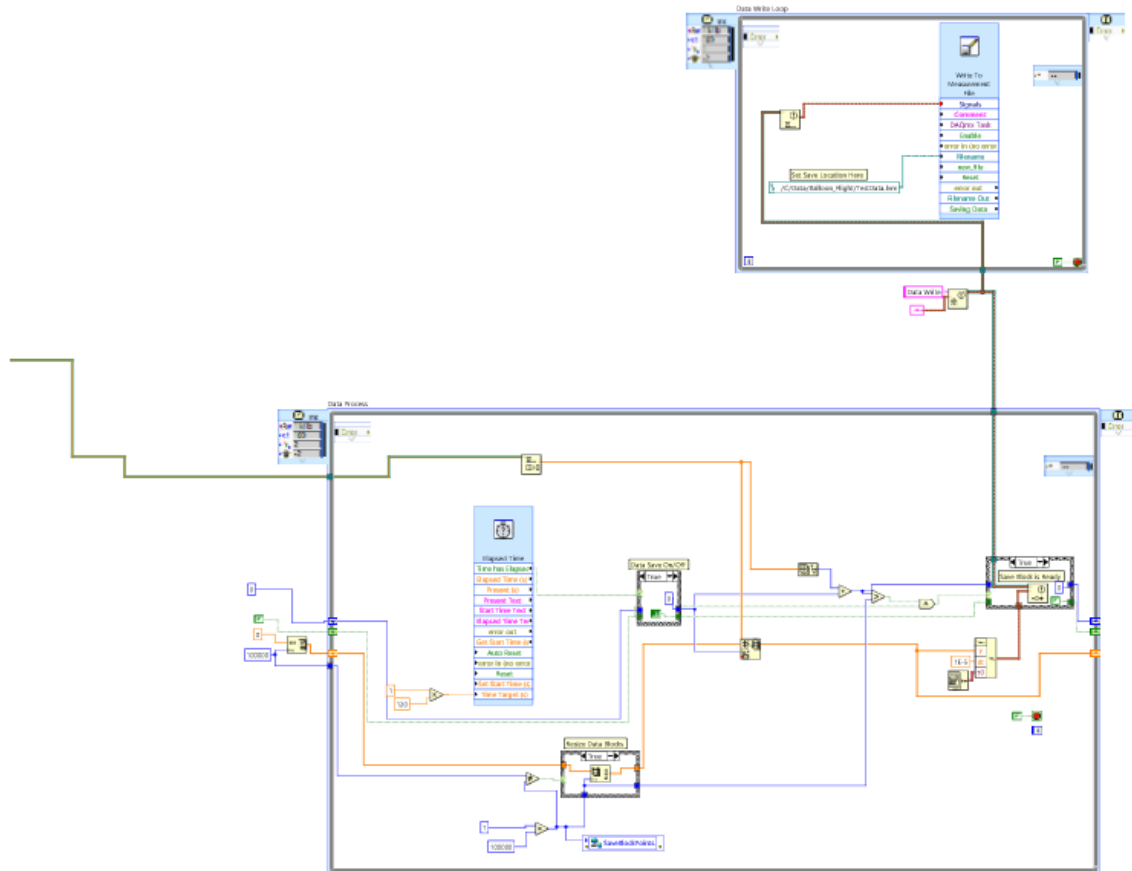
C:\Users\Mike\Desktop\cRIO - Copy\RT Main.vi

Last modified on 11/18/2016 at 1:49 PM

Printed on 12/9/2016 at 2:09 PM



RT Main.vi
C:\Users\Mike\Desktop\cRIO - Copy\RT Main.vi
Last modified on 11/18/2016 at 1:49 PM
Printed on 12/9/2016 at 2:09 PM



Matlab Flight Data Analysis Script

12/9/16 4:29 PM C:\Users\Mik...\BalloonSensor PostProc.m 1 of 12

```
%% LED Sensor Demultiplexer and post processing Code

%This code has been developed over a few years and repurposed to for different
%systems, so has seen a number of development cycles. It has also taken on
%different names (originally called LEDs.m).

%Essentially, this code was developed to demultiplex an amplitude modulated
%optical systems used in absorption sensor. After seperating the
%signals using an FFT, the code attempts to apply Beer's law with what data
%is provided.

%% Required Files

% ReadLabVIEWlvm.m

% data files containing measured data

%% Authors
%Kyle Thurmond: kthurmond@knights.ucf.edu or kylethurmond@gmail.com
%Zachary Loparo: zacharyloparo@gmail.com

%% Load data files and set parameters

close all
clear all
clc

disp('Code Begin')
% Load file for calculating the correction factors
% Folder containing data files
disp('Where is your data?:')
data_folder = uigetdir;
current_folder = pwd;

% Check whether or not it exists
prompt = 'Do you have calibration data (neat gas measurements)? (y/n)[y]: ';
keepGoing = input(prompt, 's');

if (~strcmpi(keepGoing, 'y'))
    disp('Select calibration data file:')
    clear_file = uigetfile;
    disp('Loading file...')
    [CLEAR, ~, ~, ~, ~, ~] = ReadLabVIEWlvm( clear_file );
    hasCLEAR = 1;
end

% Check whether or not it exists
prompt = 'Do you have environmental data (Excel file)? (y/n)[y]: ';
keepGoing = input(prompt, 's');
```

```

if(~strcmpi(keepGoing,'y'))
    disp('Select environmental data file:')
    env_file = uigetfile;
    disp('Loading file...')
    [~,~, environment_data] = xlsread(env_file, 'Sheet1');
end

environment_timeline = environment_data(2:end,1);

% How many bins to break it up into? default = 100; (which is 100 samples
% each for a 100kS file.)

% bins = 100;

% Uncomment to provide control of bins.
bins = input('Number of bins to use [100]: ');
if isempty(bins)
    bins = 100;
end

fprintf('\nUsing %d bins\n\n', bins);

% Frequencies of modulated LEDS
f36 = 11000;
f42 = 7000;
f47 = 5000;

% Sampling frequency (default = 100000, 100kHz)
fs = 100000;

% Expected Concentrations
co_concentration = 4.97; % in percent
co2_concentration = 5.52; % in percent

pathlength = 12.7; % in cm (5in)

% environment and DAQ time alignment
daq_time = datetime('09/01/2016 10:56 AM', 'Format', 'MM/dd/yyyy h:mm a');
env_time = datetime('09/01/2016 3:00 PM', 'Format', 'MM/dd/yyyy h:mm a');
delta_time = env_time - daq_time;

%% Set up the output file

% Prompt for output file name
prompt = 'Output File name (press enter to use default name): '; % Propmt for file name ✓
input
name = input(prompt, 's');
if isempty(name) % If not given assign default filename w/ date
    default_name = 'Results_';
    d = date;

```

```

    name = [default_name d];
end
outfile = [name, '.xlsx']; %Out file name

info = ['Creating Spreadsheet: ', outfile];
disp(info)

% Set up header info
% theader (time header) {1,1} will be used for the title, saying what the sheet contains
% (M36, BICO2, etc.)

theader{3,1} = 'File Name';
theader{4,1} = 'Comment';

% Setup the default output file (assuming steady state, same as old one)

row = 4; % Where we will begin writing data

sheet = 'Averaged Data';

header{1,2} = 'LED Amplitude';
header{1,8} = 'CO Measurement';
header{1,17} = 'CO2 Measurement';
header{1,26} = 'Environment Information';
header{1,31} = 'DAQ Information';

header{2,2} = 'LED36';
header{2,4} = 'LED42';
header{2,6} = 'LED47';
header{2,8} = 'I/I0';
header{2,13} = 'Concentration %';
header{2,18} = 'I/I0';
header{2,22} = 'Concentration %';
header{2,26} = 'Balloon CPU Time';
header{2,31} = 'DAQ Time';

header{3,1} = 'File'; % LED amplitude
header{3,2} = 'Average';
header{3,3} = 'Std. Dev.';
header{3,4} = 'Average';
header{3,5} = 'Std. Dev.';
header{3,6} = 'Average';
header{3,7} = 'Std. Dev.';

header{3,8} = 'Expected'; % CO I/Io
header{3,9} = 'Measured';
header{3,10} = '-ln(I/Io)';
header{3,11} = 'Std. Dev. of ln';
header{3,12} = '95% CI of ln';

header{3,13} = 'Expected'; % CO concentration %

```

```
header{3,14} = 'Measured';
header{3,15} = 'Std. Dev.';
header{3,16} = '95% CI';

header{3,17} = 'Expected'; % CO2 I/Io
header{3,18} = 'Measured';
header{3,19} = '-ln(I/Io)';
header{3,20} = 'Std. Dev. of ln';
header{3,21} = '95% CI of ln';

header{3,22} = 'Expected'; % CO2 concentration %
header{3,23} = 'Measured';
header{3,24} = 'Std. Dev.';
header{3,25} = '95% CI';

header{3,26} = 'Date';
header{3,27} = 'Time';
header{3,28} = 'Pressure (Torr)';
header{3,29} = 'Temperature (deg C)';
header{3,30} = 'Altitude (M)';
header{3,31} = 'Date';
header{3,32} = 'Time';
header{3,33} = 'Comment';

xlswrite(outfile,header,sheet,'A1');

%% Calculate correction Factors

% Preallocate matrices/vectors
m36 = zeros(bins,1); % One column of rows = number of bins
m42 = m36;
m47 = m36;
blCO2 = m36;
blCO = m36;
CO2 = m36;
CO = m36;
lnCO2 = m36;
lnCO = m36;

if (hasCLEAR ~= 0)
    % Set up CLEAR.dat as the file we want to process
    y = CLEAR(:,2);
    % t = CLEAR(:,1);

    N = length(CLEAR); % Number of data points in file
    nN = floor(N/bins); % Number of data points per bin.

    T = nN/fs; % period between points

    % Do initial FFT and calculation
    for i = 1:bins
```

```

yy = y((i*nN-nN)+1:i*nN); %Data segment i

mag = (2/(fs*T))*(abs(fft(yy,nN))); %FFT of data segment i

N36 = round(f36*T); %location of the LED36 signal
N42 = round(f42*T); %location of the LED42 signal
N47 = round(f47*T); %location of the LED47 signal

%Half width to make sure we pick out the correct point
hw = round(nN/100);

m36(i) = max(mag(N36-hw:N36+hw)); %LED36 amplitude
m42(i) = max(mag(N42-hw:N42+hw)); %LED42 amplitude
m47(i) = max(mag(N47-hw:N47+hw)); %LED47 amplitude

end

% Calculate the correction factors
cf42 = mean(m36)/mean(m42);
cf47 = mean(m36)/mean(m47);
else
prompt = '\nWarning: CLEAR.dat does not exist, so no correction factors are
calculated.\nCorrection factors set to -1.\n';
fprintf(prompt);
clear prompt
cf42 = -1;
cf47 = -1;
end
%% Do file iteration

thisDir = dir([data_folder '*.lvm']);

tic % Start timer to not time it takes code to run.

numfiles = 0; % Count number of files

sprintf('\nBegin File Iteration...\n');
%initialize values
time_init = 1;

for loop1 = 1:length(thisDir) % All of this for loop is from the previous code
if thisDir(loop1)..isdir
continue
else
thisFile = thisDir(loop1).name;
[thisName, thisExt] = strtok(thisFile, '.');
if strcmpi(thisExt, '.lvm') %Makes sure that we have lvm file, so as to avoid
reprocessing the .dat files.
[data, thisDate, thisTime, samples, thisComment, flag] = ReadLabVIEWlvm(
thisFile );
measurement_time = datetime([thisDate ' ' thisTime], 'Format', 'dd-MMMM-yyyy')

```

```

h:mm:ss');

    %fix NIDAQ time
    if strcmp(thisTime(1:2),'12')
        %for some stupid reason NI DAQ doesn't change the date to
        %the next day till 1am so, I am doing it manually
        measurement_time = measurement_time + duration(24,0,0);
    end
    numfiles = numfiles+1;

    else
        continue
    end
end
disp(['Processing file ' thisFile])
y = data(:,2);
%   t = data(:,1);

N = length(data);
nN = floor(N/bins);

T= nN/fs;

%plot of the fft of signal at specific bin size based no sampling frequency

%%figure1 = figure;

% Create axes
%%axes1 = axes('Parent',figure1,'XMinorTick','on','XMinorGrid','on','XGrid','on');

%%box(axes1,'on');
%%hold(axes1,'all');

m36 = zeros(bins,1);
m42 = m36;
m47 = m36;

%% Compute FFT and calculate magnitudes, averages.

for i=1:bins % Actual FFT calculations
    yy = y((i*nN-nN)+1:i*nN); %data segment i

    mag = (2/(fs*T))*(abs(fft(yy,nN))); %FFT for data segment i

    %plot((1/T)*(0:nN-1), mag);

    N36 = round(f36*T); %location of the LED36 signal
    N42 = round(f42*T); %location of the LED42 signal
    N47 = round(f47*T); %location of the LED47 signal

    %Half width to make sure we pick out the correct point

```

```
hw = round(nN/100);

m36(i) = max(mag(N36-hw:N36+hw)); %LED36 amplitude
m42(i) = max(mag(N42-hw:N42+hw)); %LED42 amplitude
m47(i) = max(mag(N47-hw:N47+hw)); %LED47 amplitude

blCO2(i) = m42(i)*cf42/m36(i); %L42/L36
blCO(i) = m47(i)*cf47/m36(i); %L47/L36

lnCO2 = -log(blCO2); % take -ln of them.
lnCO = -log(blCO);

% Doesn't follow BL law so for now not needed.
% CO2(i) = log(blCO2(i))/-kCO2; %CO2 concentration using Beer's
% CO(i) = log(blCO(i))/-kCO; %CO2 concentration using Beer's
end
%% Rest of loop, saving the data
%calculate averages
avg36 = mean(m36);
avg42 = mean(m42);
avg47 = mean(m47);

avgblCO2 = mean(blCO2);
% avgCO2 = mean(CO2);

avgblCO = mean(blCO);
% avgCO = mean(CO);

avglnCO = mean(lnCO);
avglnCO2 = mean(lnCO2);

%Calculate std. dev.
sd36 = std(m36);
sd42 = std(m42);
sd47 = std(m47);

sdlnCO2 = std(lnCO2);
% sdCO2 = std(CO2);

sdlnCO = std(lnCO);
% sdCO = std(CO);
```

```

% Save the loop data to some variables
avg_36(numfiles) = avg36;
avg_42(numfiles) = avg42;
avg_47(numfiles) = avg47;

sd_36(numfiles) = sd36;
sd_42(numfiles) = sd42;
sd_47(numfiles) = sd47;
sd_lnCO(numfiles) = sdlnCO;
sd_lnCO2(numfiles) = sdlnCO2;

avg_blCO(numfiles) = avgblCO;
avg_blCO2(numfiles) = avgblCO2;
avg_lnCO(numfiles) = avglnCO;
avg_lnCO2(numfiles) = avglnCO2;

% Save the time dependent data for each loop
M36(:,numfiles) = m36;
M42(:,numfiles) = m42;
M47(:,numfiles) = m47;

BLCO(:,numfiles) = blCO;
BLCO2(:,numfiles) = blCO2;

LNCO(:,numfiles) = lnCO;
LNCO2(:,numfiles) = lnCO2;

% Save the header information that we want
theadr{3,numfiles+1} = thisFile; % store file name
theadr{4,numfiles+1} = char(thisComment);

%% Get Environment Data
display('Retriev environmental data...')
for time_index = time_init:length(environment_timeline)
    balloon_time = datetime(environment_timeline{time_index}, 'Format','MM/dd/yyyy h:mm:ss aa');

    if (measurement_time + delta_time) == balloon_time
        pressure = environment_data{time_index+1,22};
        temperature = environment_data{time_index+1,32};
        altitude = 0;
        time_init = time_index; % reduce the number of loops next iteration
        break
    else
        pressure = 0;
        temperature = 0;
        altitude = 0;
        balloon_time = 0;
    end
end
end

```

```

%% Write averaged data to file

writeRow{1} = thisFile;
writeRow{2} = avg36;
writeRow{3} = sd36;
writeRow{4} = avg42;
writeRow{5} = sd42;
writeRow{6} = avg47;
writeRow{7} = sd47;

writeRow{9} = avgblCO;
writeRow{10} = avglnCO;    % of the ln
writeRow{11} = sdlnCO;
writeRow{12} = 1.96*sdlnCO; %1.96 is for the 95%CI.

writeRow{13} = co_concentration; %1.96 is for the 95%CI.

writeRow{18} = avgblCO2;
writeRow{19} = avglnCO2;    % of the ln
writeRow{20} = sdlnCO2;
writeRow{21} = 1.96*sdlnCO2;

writeRow{22} = co2_concentration;
if isnumeric(balloon_time)
    writeRow{26} = 'No correlated balloon measurement';
    writeRow{27} = 0;
else
    writeRow{26} = char(datetime(balloon_time, 'Format','dd-MMMM-yyyy'));
    writeRow{27} = char(datetime(balloon_time, 'Format','HH:mm:ss'));
end
writeRow{28} = pressure;
writeRow{29} = temperature;
writeRow{30} = altitude;

writeRow{31} = char(datetime(measurement_time, 'Format','dd-MMMM-yyyy'));
writeRow{32} = char(datetime(measurement_time, 'Format','HH:mm:ss'));
writeRow{33} = char(thisComment);

display('Write data...')
xlswrite(outfile,writeRow,sheet,['A' num2str(row)]);
row = row + 1;
toc
end
%% Record correction factors

% Add a line saying what the correction factors were.
row = row + 1; % move a few rows down

cfdat{1,1} = 'Correction Factors'; %Headings
cfdat{2,1} = 'cf42';
cfdat{2,2} = 'cf47';

```

```
cfdat{3,1} = cf42; % The correction factors
cfdat{3,2} = cf47;

xlswrite(outfile,cfdat,sheet,['A' num2str(row)]);

%% Write the other sheets

% prompt = 'Save the time data? y/n [n]: ';
% saveTimeData = input(prompt, 's');
% if isempty(saveTimeData)
%     saveTimeData = 'n';
% end
%
% if strcmpi(saveTimeData,'n') %delete the time data if we don't want it
%     clear BLCO BLCO2 LNCO LNCO2 M36 M42 M47
% end
%
% if ~strcmpi(saveTimeData,'n')
%
% % M36
% thisData = M36;
% pagename = 'M36';
%
% sheet = pagename;
% theader{1,1} = pagename;
% xlswrite(outfile,theader,sheet,'A1');
% xlswrite(outfile,thisData,sheet,'B5');
%
% % M42
% thisData = M42;
% pagename = 'M42';
%
% sheet = pagename;
% theader{1,1} = pagename;
% xlswrite(outfile,theader,sheet,'A1');
% xlswrite(outfile,thisData,sheet,'B5');
%
% % M47
% thisData = M47;
% pagename = 'M47';
%
% sheet = pagename;
% theader{1,1} = pagename;
% xlswrite(outfile,theader,sheet,'A1');
% xlswrite(outfile,thisData,sheet,'B5');
%
%
% % BLCO
% thisData = BLCO;
% pagename = 'BLCO';
%
```

```

% sheet = pagename;
% theader{1,1} = pagename;
% xlswrite(outfile,theader,sheet,'A1');
% xlswrite(outfile,thisData,sheet,'B5');
%
% % BLCO2
% thisData = BLCO2;
% pagename = 'BLCO2';
%
% sheet = pagename;
% theader{1,1} = pagename;
% xlswrite(outfile,theader,sheet,'A1');
% xlswrite(outfile,thisData,sheet,'B5');
%
%
% % LNCO
% thisData = LNCO;
% pagename = 'LNCO';
%
% sheet = pagename;
% theader{1,1} = pagename;
% xlswrite(outfile,theader,sheet,'A1');
% xlswrite(outfile,thisData,sheet,'B5');
%
%
% % LNCO2
% thisData = LNCO2;
% pagename = 'LNCO2';
%
% sheet = pagename;
% theader{1,1} = pagename;
% xlswrite(outfile,theader,sheet,'A1');
% xlswrite(outfile,thisData,sheet,'B5');
%
% end

%% Clear unneeded variables

clear CO CO2 N N36 N42 N47 T ans avg36 avg42 avg47 avgb1CO avgb1CO2
clear avglncO avglncO2 bins cfdat data f36 f42 f47 flag freq fs
clear header hw i info j loopl m mag n nN numfiles CLEAR
clear pagename prompt q row samples saveTimeData blCO2 blCO
clear sdlnCO sdlnCO2 sheet str t thisComment thisData thisDate
clear thisDir thisExt thisFile thisName thisTime writeRow xmax y yy
clear lnCO lnCO2 m36 m42 m47

save(name); % Save the useful stuff to a matlab variable set for future

disp('Saving the variables to a matlab workspace')

clear name outfile

```

12/9/16 4:29 PM C:\Users\Mik...\BalloonSensor PostProc.m 12 of 12

disp('END CODE')